Supplementary Materials for

Perovskite-perovskite-silicon triple junction solar cells with improved carrier and photon management

Artuk *et al.*

Corresponding authors: Kerem Artuk, kerem.artuk@epfl.ch; Christian M. Wolff, christian.wolff@epfl.ch

The PDF file includes:

Supplementary Note 1. Development of the middle-cell absorber

Perovskite solar cells with ~1.54 eV Pb-based absorbers with the composition $Cs_{0.05}FA_{0.90}MA_{0.05}PbI_3$ (+5% $MAPbCl_3$) absorber have demonstrated exceptional performance, delivering efficiencies above ~ 26% in multiple studies (*20*, *21*). Here, control ~ 650-nm-thick cells (**Fig.2(c)**) with this MBG absorber exhibited a PCE of around 23% (**Fig.2(d)**). While V_{OC} reached 1.18 V and FF >83%, the current density remained limited to ~23 mA/cm². Initial attempts to increase the absorber thickness by adjusting the solution molarity and spin-coating parameters resulted in delamination of the absorber upon annealing, as shown in Fig. **S22**. This issue arose due to increased mechanical stress and weak adhesion between the perovskite and the hydrophobic Me-4PACz hole transport layer (*22*). While exploring alternative self-assembled monolayers (SAMs), such as 2PACz and 4PADCB, that mitigated the delamination issue, the performance of devices with thicker absorbers was still inferior to that of the control devices (see **Fig.S23).** That is why we propose another strategy to increase the thickness of the absorber, a three-step deposition method.

Materials and Methods

Perovskite fabrication & deposition

1. Wide bandgap absorber

WBG absorber utilized in this work is $Cs_{0.22}FA_{0.78}Pb(I_{0.60}Br_{0.30}Cl_{0.10})_3$. The bandgap is tuned by adjusting the Br ratio between 30 to 40%. The chloride amount is fixed at 10%. By adjusting the molarity between 1M to 1.2M, the thickness is also tuned. The 1M perovskite solution is prepared by mixing, 0.707M PbI_2, 0.1M $PbCl_2$, 0.3M PbBr2, 0.1M MACl, 0.78M FAI, 0.3M FABr, 0.22M CsI in DMF:DMSO 3:1 (volume ratio). The solution is shaken for at least 1 hour to make sure the precursors are dissolved. Then additives from the stock solution (e.g., 10 mg/mL in DMF:DMSO) are added into the perovskite ink and shaken at least 15 min. Whole solution is filtered using 0.22 um PTFE filters. The absorber is fabricated with the one-step antisolvent method. The precursor solution (100 µL) is spread onto the substrate (2.5 *x* 2.5cm^2), then spun at 5000 rpm with 1000 rpm/s for 32 s. When 10 s are left during the spin-program, 200 µL of Anisole is dropped onto the substrate. Then the samples are annealed at 100°C for 15 min inside the glovebox.

2. Medium bandgap absorber – one-step

The medium bandgap (MBG) absorber utilized in this work is $Cs_{0.05}FA_{0.9}MA_{0.05}PbI_3$ and 5% excess $MAPbCl_3$. The solution is prepared by mixing, 1.61M PbI_2, 0.048M $PbCl_2$, 0.08M MAI, 0.2M MACl, 1.43M FAI, 0.08M CsI in DMF:DMSO 4:1 (volume ratio). The solution is shaken at least 1 hour to make sure the precursors are dissolved and then filtered using 0.22 µm PTFE filters. The absorber is fabricated with the one-step antisolvent method. The precursor solution (100 µL) is spread onto the substrate (2.5 *x* 2.5cm^2), then spun at 3000 rpm with 300 rpm/s for 40 s. When 10 s are left during the spin-program, 250 µL of Anisole is dropped onto the substrate. Then the samples are annealed at 100°C for 15-20 min inside the glovebox.

3. Three-step absorber fabrication

Upon fabrication of one-step perovskite absorber with anti-solvent method, the samples are loaded into Lesker evaporation chamber. Inorganic halide template consisting of 180 nm PbI_2 and 3 nm CsI is co-evaporated onto the one-step absorber with 1A/s and 0.015 A/s rates. Then, organohalides (0.3M FAI:MAI with 95:05 ratio in IPA and 2.5 mg/mL as additive) is spin-coated dynamically at 4000 rpm for 30s. To form the three-step absorbers, samples are annealed at 100°C for 10 min.

Solar cell fabrication

Fabrication of single-junction perovskite solar cells

0.7 mm ITO (15 ohm/square - TKing) coated glass substrates are cleaned with Helmanexx and DI respectively using ultrasonic baths for 15 min. Samples are exposed to UV-ozone for 30 min right before the SAM deposition. SAM (e.g., Me-4PACz) solution (1 mg/mL) is spin-coated onto substrates for 100 µL with a program of 10 s resting time, 3000 rpm, 300 rpm/s. Then the substrates are annealed for 10 min at 115°C. To improve the wetting, 0.25% SiOx-np solution in Ethanol (for WBG) and 0.1% SiOx-np for MBG in EtOH (20 nm diameter) spin-coated for 100 µL with a program of 2000 rpm with 500 rpm/s for 30 s and annealed at 115 °C for 10 (*1*).

Interface passivation

For the MBG 0.5 mg/mL $PDAI_2$ in IPA is dynamically spun at 6000, followed by annealing at 100 °C for 5 min utilized.

For the BMP in WBG, 0.4 mg/mL PCl is dynamically spun at 6000 rpm and annealed at 100 °C for 5 min. After cooling down, 0.5 mg/mL 4F-PEACl is dynamically spun at 6000 rpm and annealed at 100 °C for 5 min.

Top-electrode stack

25 nm of C_{60} (Creaphys or NanoC, >99.9% - resublimed) is deposited via thermal evaporation with a rate of 0.2 A/s in the Angstrom thermal evaporator. Then ALD-SnO_x is deposited at 95-100°C with pulse purge times of 0.3s / 6s / 0.1s / 6s for 150-175 cycles with TDMASn and H_2O sources. The utilized thicknesses for baseline devices are 20-22.5 nm measured with an ellipsometer on c-Si. For the metal contact, 150 nm of Ag is deposited via thermal evaporation with a rate of 1.5-2 A/s. The device's active area is 0.2 cm^2.

Fabrication of monolithic MBG-silicon heterojunction tandem solar cells – 1cm^2

The bottom cell fabrication process is performed on 200 µm-thick n-type, 2 ohm.cm, FZ Si wafers. For the front-flat devices, a layer of SiNx is applied to the front side using PECVD, and the rear side is textured using a KOH solution to create a random pyramid pattern. The SiNx masking layer is then removed and samples undergo a cleaning sequence prior PECVD process. For the double-side nanotextured devices, KOH solution with an additive is utilized to create sub-micron textured pyramids.

Through PECVD, hydrogenated amorphous Si layers are deposited on both sides. On the front side, a-Si:H(i), a-Si:H(n) are deposited at 200°C. On the rear side, a-Si:H(i) and a-Si:H(p) is deposited at 200°C (45. On the rear side, an 80 nm-thick ITO and 500-600 nm thick Ag layer is deposited by sputtering through a shadow mask. The front side is completed by sputtering a 20 nm-thick ITO layer for interconnection. As the final step before top cell processing, 4" wafers are then laser-cut into 2.5 *x* 2.5 cm^2 substrates, which are annealed at 210°C for 15 min in ambient to recover the sputter-induced damage.

1:1 mixture of Me-4PACz (1mg/mL in Ethanol - TCI) and 4PADBC (1mg/mL in Ethanol - Dyenamo) is spin-coated statically at 3000 rpm for 30 s with 10 s resting time, followed by an annealing at 125°C for 10 min. To construct the middle-reflector, 0.25 to 0.5% wt. SiOx-np (~20 nm diameter) in Ethanol is spin-coated statically at 2000 rpm with 500 rpm/s acceleration, followed by an annealing step of 10 min at 125°C. Either one-step or three-step absorbers are utilized for MBG-Si tandems with recipes given above. For MBG, $PDAI_2$ passivation is utilized with the recipes given above. The thickness of C_{60} is reduced down to 15-20 nm for the tandem devices, and 150-175 cycles of ALD-SnO_x is used in tandems. After the ALD-SnO_x, 30-35 nm of IZrO with sheet resistance around 250 ohm/square is deposited from 4-inch 98% I_2O_3 + 2% ZrO target with deposition power of 70W and working pressure 2.7 µbar with ~0.14% of O_2 to Ar ratio. After the TCO, ~500 nm of Ag grid is evaporated with a rate of 2 Å/s which is followed by 100 nm of NaF with 1 Å/s rate.

Fabrication of triple junction solar cells

Fabrication of the bottom-cell is similar to the MBG-Si tandems. For the middle-cell, the C_{60} thickness is increased to 30 nm, and the number of cycles of SnOx is increased to 300. The goal of utilizing thicker interconnection films (C_{60}, SnO_x) is to improve the barrier properties. For the interconnection layer, 15 nm

of IZO is deposited with a mask of 1.3 cm *x* 1.3 cm. For the top-cell, 1:1 mixture of Me-4PACz:2PACz (1mg/mL) in Ethanol is utilized. 100 µL mixed SAM solution is spun statically with 5 s resting time at 3000 rpm for 30 s followed by an annealing at 95°C for 5 min. To improve the wetting, 0.25% SiOx-np is spun statically at 2000 rpm for 30 s followed by an annealing at 95°C for 5 min. 100 µL CsFA-TH perovskite solution is spread and spun at 5000 rpm with 1000 rpm/s acceleration for 35 seconds. Last 10 seconds 200 µL of Anisole is dropped on the substrate. Samples are annealed at 100°C for 10 min. For the interface passivation, the exact procedure mentioned above is applied. 15 nm of C_{60}, 20 nm of SnOx and 25-30 nm of IZrO with sheet resistance around 350 ohm/square and 500 nm of Ag are deposited as the negative electrode stack. 110 nm of NaF is deposited as an anti-reflective coating.

Characterization

Density Functional Theory

Density functional theory calculations are performed with the electronic structure code VASP (*3*, *4*). We use the C_GW_new, N_GW_new, O_GW_new, H_GW_new, Pb_d_GW, Cs_sv_GW, and I_GW PAW pseudo-potentials (*3*) as distributed with vasp.6.4.2. Furthermore, the calculations use a plane-wave cutoff of 750 eV (ENCUT in VASP), and simulation boxes of dimensions 20 Å x 20 Å x 20 Å. Geometries are fully relaxed using the r^{2}SCAN+rVV10 density functional (*5*), which combines the regularized-restored version (*6*, *7*) of the SCAN meta-GGA functional (*8*, *9*) with the rVV10 van-der-Waals correction (*10*, *11*) . We use *b*=11.95 for the rVV10 parameter as suggested by Ning *et al.* (*5*). Calculations are performed in vacuum, and we neglect spin-orbit coupling corrections and vibrational contributions to the binding energies.

Table.S1 sums up the calculated binding energies. Structures showing adsorption of Pb^{2+} ions to HBA are given in Fig. 1 of the main text. We employ the Makov-Payne correction (*12*) to handle long-range electrostatic interactions between periodic images. We found that the remaining errors closely follow a $1/L^3$ behavior (L being the box length), and we use this to extrapolate the adsorption energies to infinite L. Using the same extrapolation procedure, we have also investigated the adsorption of FA^+ and Cs^+ cations to HBA. The binding motive for Cs^+ is the same as for the case of Pb^{2+}, that is via formation of Cs-N bonds (not shown). FA^+ also prefers the same binding site, molecular structures are shown in **Fig.S6** (a)-(c). For interaction of a (neutral) $CsPbI_3$ molecule with HBA, the chosen 20 Å x 20 Å x 20 Å box is large enough to reduce the finite size error well below 0.1 eV. Binding energies are given with respect to isolated HBA and $CsPbI_3$ molecules. In the isolated $CsPbI_3$ molecule, Pb and Cs are coordinated via three shared I-bonds). $CsPbI_3$ can simply attach to HBA by occupying the aforementioned cationic binding site, forming a Cs-N bond. This is the most stable configuration for 3-HBA and 4-HBA, see **Fig.S6** (e) and (f). Such a binding motive exists also for 2-HBA as a metastable state. However, due to the spatial proximity of the NH_2 and OH groups in 2-HBA, $CsPbI_3$ can interact with both of them simultaneously, see **Fig.S6** (d) (notice also the rotation of the OH group). This slightly increases the adsorption energy from 1.0 eV to 1.2 eV, see **Table.S1**.

Table.S1 Calculated binding energies for HBA interacting with Pb^{2+}, FA^+ and Cs^+ ions, as well as with a $CsPbI_3$ molecule.

	2-HBA	3-HBA	4-HBA
Pb^{2+}	6.8 eV	6.8 eV	6.8 eV
FA^+	1.7 eV	1.6 eV	1.6 eV
Cs^+	1.3 eV	1.2 eV	1.2 eV

$CsPbI_3$	1.2 eV	1.0 eV	1.0 eV

JV

The 4PP measurement method is used. JV measurements were obtained using a two-lamp (Halogen and Xenon) class AAA WACOM sun simulator with an AM1.5G irradiance spectrum at 1.000 W/m2. 0.1 cm^2 shadow masks are used to measure cells with an area of 0.2 cm^2 unless otherwise stated. Opaque devices are illuminated from the glass side. The single junction cells are measured with a scan rate of ~ 0.50V/s, first, reverse scan, and then forward scan. Both reverse and forward scans are included in the JV statistic plots. Three-point weight MPP measurements are performed using an in-house written LabVIEW code. For the measurement of tandem and triple junction devices, before each measurement, the calibration of the AAA WACOM system is adjusted with three different certified cells with different spectral responses to minimize the spectral mismatch of the sources. Initially, to adjust the intensity of the Xe lamp, a calibrated encapsulated cell (WPVS – blue cell) containing a monocrystalline silicon solar cell, which is covered with a KG5-filter was used. Then to adjust the intensity of Ha lamp, a calibrated encapsulated cell (WPVS – red cell) containing a monocrystalline silicon solar cell, which is covered with a RG780-filter was used. Then, overall spectrum is checked with a calibrated encapsulated cell (WPVS without filter broadband – black cell). All calibrated Si cells are provided by Fraunhofer ISE. Then the cells with ~1 cm^2 are measured with a scan rate of ~ 0.1V/s and a similar MPP tracking algorithm is utilized as the single junction perovskite solar cells. A temperature-controlled (25 ºC) brass chuck was used.

EQE

EQE spectra were measured with a custom-made spectral response set-up where the samples were irradiated with chopped light at a frequency of ~200 Hz and the response was measured with a lock-in amplifier. For tandem cells visible and IR light biases are used to saturate complementary sub-cells and to measure each sub-cell near short-circuit conditions 0.6V and 1.1V bias voltages are applied to the cell when measuring top and bottom cells respectively.

EQEs of the triple junctions are measured full-area including shadowing from the fingers using Pv-tools LOANA system. For the measurement of triple junction devices, the signal in the junction that is measured is maximized and other junctions is minimized by adjusting light and voltage bias. For example, while measuring the top-cell, signal in the top-cell (e.g., at 550 nm) is maximized by adjusting the voltage bias (e.g., 0.5 to 2V) and light bias (e.g., IR LED), and middle-cell and bottom-cell is minimized (e.g., 1000 nm). For the middle-cell, 0.5 to 2V voltage range is utilized with Blue LEDs. For the bottom-cell, 0.5V to 2V voltage range is utilized with Blue LEDs with white light.

JV and EQE in Fraunhofer ISE

EQEs were measured with an in-house measurement setup containing a Xenon lamp as a light source. The light is chopped at ~133 Hz and directed through a double grating monochromator to produce monochromatic light. A transimpedance amplifier provides a bias voltage during the measurements and strengthens the signal, which is then detected by a lock-in amplifier. Selective infrared and red LEDs (940 nm and 740 nm, respectively) were used for the measurement of the perovskite top cell. Blue (460 nm) and infrared LEDs were employed for the measurement of the perovskite middle cell. The silicon bottom cell was measured under selective blue and red LEDs. A bias voltage was applied to the device for each sub-cell measurement, following the international standard procedure (*13*). The EQE was recorded in 10 nm increments and the temperature was maintained at 25 ℃.

The JV measurements of triple junction solar cells were conducted using a Wavelabs SINUS 220 light-emitting diode (LED)-based solar simulator containing 20 different LED channels. The spectral responses (SR) were measured prior to the JV measurement. The spectrum was then calculated using the relative SRs according to the procedure described in (*14*). This ensures that the spectrum is correctly adjusted such that the photocurrent generated by each sub-cell under the simulator spectrum matches the photocurrent generated under the AM1.5g spectrum (*15*, *16*). The JV curves were then measured from 3200 mV up to 0 mV with a voltage step of 10 mV and a scan rate of ~0.1V/s first in reserve, then in forward scan direction. The temperature of the measurement chuck was maintained at 25 °C.

Long-term stability

Cicci Research stability measurement setup is utilized where the samples are kept in N_2 atmosphere, under 1-sun illumination by tracking the MPP with the perturb & observe algorithm. The N_2 chambers are temperature controlled, and cells saturate ~10-15°C higher than the chamber temperature.

For stability testing for WBG devices in MPP, 2PACz HTL and no perovskite-C60 interface passivation is utilized, for simplicity.

Outdoor testing

To evaluate the field performance of the encapsulated 3J cells, time series data were analyzed from two devices tested outdoors in Neuchâtel, Switzerland, between February 6 and June 3, 2025. sGlobal horizontal irradiance (GHI) was measured using a pyranometer co-located with the test setup.

The performance ratio (PR) was computed and analyzed over time to extract long-term trends and identify potential anomalies. The PR is a dimensionless metric that compares the actual output to its expected output under standard test conditions (STC). It normalizes the device's power output by both its nominal rating and the incident irradiance, and is defined as:

$$PR(t) = \frac{P_{MPP}(t)/P_{nom}}{G(t)/G_{STC}}$$

Where $P_{MPP}(t)$ is the maximum power point measured at time t (in mW), P_{nom} is the nominal power rating of the device under STC, $G(t)$ is the measured irradiance at time t (in W/m²), G_{STC} is the reference irradiance under standard conditions (1000 W/m²).

PR values outside the plausible range (i.e., below 0.3 or above 1.3) were excluded to filter out erroneous data and outliers. To study temporal evolution, the 10-minute PR values were aggregated into daily statistics. For each day, the average PR was calculated along with its day-to-day variability, using standard deviation as a measure of spread. To reduce noise in the daily data and emphasize long-term behavior, a Gaussian smoothing filter was applied to the daily PR averages ($\sigma = 8$), to effectively smooth out short-term fluctuations while preserving broader performance patterns over time. Additionally, confidence intervals were added above and below the smoothed trendline using the daily standard deviation.

HDR-EQE

High-dynamic range external quantum efficiency (HDR-EQE) measurements were conducted using a home-built setup. Here, the output of a Tungsten-Halogen light source (Thorlabs, SLS201L) was fiber-coupled into a Monochromator-F system (Technologie Manufaktor). The monochromator fiber output light

was collimated and physically chopped at 273 Hz (Thorlabs, MC2000B), and different optical components were used to guide the light onto the device under test (DUT). Various long- and short-pass filters from Thorlabs and Edmund Optics were used to suppress optical noise and parasitic stray light. The DUT photocurrent signal was first amplified by a current amplifier with variable gain up to 10^9 V/A (Femto, DLPCA-200) before being analyzed with a lock-in amplifier (Stanford Research, SR865A). During the measurement, the DUTs were under constant dry nitrogen flow. Prior EQE measurements, the system was calibrated using a NIST-calibrated Silicon (Newport, 818-UV) and Germanium (Newport, 818-IR) reference photodiode. Electrical bandwidths of up to 1 MHz were used for sub-bandgap EQE measurements.

Transient absorption measurements

Femtosecond TA measurements were performed in a HARPIA commercial instrument (Light Conversion) equipped with Kymera 193i spectrometer (Oxford Instruments) and a broadband Si NMOS detector (Hamamatsu S3901 + C7884). An amplified 260 fs pulse train, centered at 1026 nm, with an average power of 20 W and a repetition rate of 50 kHz was generated from a Pharos Yb:KGW laser (Light Conversion). The pulse train was divided into three parts. An optical parametric amplifier (Orpheus, Light Conversion) was pumped with 17.5 W and generated a pulse train centered at 640 nm, this train served as the pump pulse and was further modulated at 40 Hz. The pump beam profile was measured with the knife-edge method yielding a FWHM of 2.68 mm from an error function fit. The pump intensity was adjusted to yield an irradiance per pulse of 50 nJ/cm^2. For the probe pulse, 0.5 W of the initial 1026 nm pulse train was routed to a motorized delay stage, providing 7 ns of delay, a white light supercontinuum was generated by attenuating it with a variable neutral density filter and focusing it into a YAG crystal. The remaining 2 W were not used in the experiment. The probe beam was focused onto the sample with a couple of parabolic mirrors and overlapped spatially and temporally with the pump pulse. All experiments were performed at room temperature.

SEM

SEM images were acquired with acceleration voltages ranging from 1 to 5 kV using either an Everhart-Thornley or an in-lens detector (JEOL JSM-7500TFE or Zeiss NVision 40 microscopes).

Steady-state PL

Custom built steady state PL setup is utilized to measure in-situ PL and PLQY. The light from the laser diode is coupled into a fiber directed into the integrating sphere and sample is illuminated. Then the emission from the sample is homogenized by multiple reflections within the integrating sphere and coupled out into another fiber that is connected to a spectrometer. As long as the emission (600 nm to 825 nm) and the excitation (532 nm) are well separated, a careful comparison of the peaks enables to measure PLQY (down to 10^{-6}). An OD filter wheel helps to change the light intensity in between 0.01 sun to 3 sun. As a calibration check, three fluorescent test samples with high specified PLQY (~70%) supplied from Hamamatsu Photonics where measured where the specified value could be accurately reproduced within a small relative error of less than 5%. For QFLS measurements the light intensity is tuned to 1-sun depending on the bandgap of the absorber using an external c-Si photodetector.

iVoc imaging

A commercial measurement system developed by Fraunhofer ISE and manufactured by Intego GmbH was used to measure the PL images. A laser with a peak wavelength of 450 nm, an LED with a peak wavelength of 700 nm, and a laser with a peak wavelength of 808 nm were used to selectively excite the sub-cells. Optical filters (transmissive range 600 nm to 650 nm for the top solar cell, 788 nm to 812 nm for the middle

solar cell, and 950 nm to 1000 nm for the bottom solar cell) were used to separate the luminescence signal from the sub-cells, before it was captured in a silicon charge-coupled device camera. The relative EQEs were used to calculate the one-sun-equivalent illumination intensities of the two lasers following the approach described by Meusel *et al.* (*16*). The intensity of the 700 nm LED was roughly adjusted (here we note a possibility of +35 mV overestimation in the middle cell iVoc) using a silicon reference solar cell. The PL images were calibrated to obtain iV_{OC} images following the approach described by Fischer, Bui *et al.*(*17*) adapted to triple-junction solar cells.

XPS/UPS

XPS measurements were performed using an Axis Supra (Kratos Analytical) with a monochromatic Al Kα X-ray line. The pass energy was set to 20 eV with a step size of 0.1 eV for XPS, and to 40 eV with a step size of 0.15 eV for AR-XPS. The emission current was set to 15 mA. The samples were electrically grounded to limit charging effects. UPS was measured using a He I UV source, with the pass energy set at 10 eV and a step size of 0.025 eV. the intensity of the UV source together with the measurement area was selected in order to prevent the energy analyzer from saturating. Secondary electron cutoff (SECO) was used to assign the work function of the material, while the valence band onset, was used to estimate the valence band maximum with respect to the Fermi level.

Grazing Incidence Wide Angle X-ray Scattering (GIWAXS)

GIWAXS experiments were performed at NCD-SWEET beamline at the ALBA synchrotron light source (Spain). An *in vacuo* undulator (IVU21) generates a low divergence X-ray beam that was monochromatized at 12.95 keV with a Si (111) channel cut monochromator. After the beam defining slits, the X-ray beam is collimated using an array of beryllium compound refractive lenses (CRLs), obtaining a beam size at the sample position of 20×80 μm^2 (FWHM: H×V). The sample was positioned on the rotation point of a Huber® double semicircle located on a complete translation stages tower which allowed precise tilts and movements of the sample. A Rayonix LX255-HS area detector (88.54 × 88.54 μm^2 pixel size for the binning mode used of 2 × 2) was used to record the scattered radiation. The reciprocal space was calibrated using Cr_2O_3 from NIST, obtaining a sample to detector of 230 mm. Data was reduced using a home-built programmed routine based on PyFAI (*18*). *In situ* spin coating during GIWAXS data collection was performed using a brushless motor (Mclennan BLDC 48) with a 0-5V speed control, calibrating the rotation speed with the integrated frequency generator. The spinner was covered with a 3D printed cover to ensure an inert N_2 atmosphere with Kapton® windows. The solution injection was remotely controlled using a Symax Spetec syringe pump, injecting 150 µL and setting a rotation speed of 2000 r.p.m. For the in situ annealing experiments, the sample temperature was controlled using a linkam stage and the sample was under continuous N2 gas flow during the in-situ measurements.

NMR

1H NMR spectra were recorded on a Bruker AV4 spectrometer (1H: 400.1 MHz) equipped with a 5 mm BBO probe at 298 K. Spectra were acquired with a 30° pulse of 3.3 µs, a spectral width of 7.8 kHz (20 ppm), an acquisition time (aq) of 4 s, a preparation delay (d1) of 1 s, and between 16 and 128 accumulations. The free induction decays were zero-filled to 65 K points and multiplied by a 0.3 Hz exponential line-broadening function prior to Fourier transformation to the frequency domain. 1H Chemical shifts were referenced to TMS using the signals of the residual protons of the deuterated solvent (δ1H = 2.50 ppm (DMSO-d6)) as secondary reference

Finite element simulations

Finite element simulations were performed using the commercially available software Comsol. The simulated tandem stack from top to bottom is NaF/IZrO/SnO_x/C_{60}/Perovskite/SiOx-np/ITO/Si with the respective layer thicknesses being 110 nm/30 nm/20 nm/15 nm/500 nm/0 nm – 150 nm/20 nm/200 µm. This stack was implemented in a 2D geometry, where the Si top structure was approximated as periodic triangles with a height of 260 nm and a base angle of 54.7° whose valleys are filled by circular NPs. The perovskite height is adjusted according to the NP filling height to maintain the volume. Using the Electromagnetic Waves module in Comsol, which solves the wave equation numerically for the given stack with supplied boundary conditions, the wavelength of the incoming light is varied. For each wavelength, the EQE of a layer is calculated by integrating over the absorption of each of its mesh points and dividing by the input power.

TOF-SIMS

ToF-SIMS measurement were performed with a time-of-flight secondary ion mass spectrometer (ToF-SIMS V system, ION-TOF). The primary beam was 25 keV Bi^{3+} with a total current of 0.46 pA and a raster size of 50 × 50 μm^2. Cs^+ ions were used with 1000 eV ion energy, 24 nA pulse current on a 400 × 400 μm^2 raster size to bombard and etch the film. The collected secondary ion spectra were normalized to the total counts.

XRD

X-ray diffraction was performed in Bragg Brentano geometry with a copper Kα source with a Kβ filter using a PANalytical Xpert Pro MPD.

Numerical calculations based on equivalent circuit modeling

Table.S2
Input parameters and PV performance parameter results of numerical calculations.

Condition	Rs total (ohm.cm^2)	Top-cell current (mA/cm^2)	Middle-cell current (mA/cm^2)	Bottom-cell current (mA/cm^2)	V_{OC} (V)	J_{SC}(mA/cm^2)	FF (%)	PCE (%)
Baseline	13.5	12.75	11.00	17.00	3.110	11.018	86.23	29.55
Rs + 1 ohm.cm^2	14.5	12.75	11.00	17.00	3.110	11.018	85.90	29.44
3-step absorbers	14.5	12.75	11.75	16.25	3.110	11.767	84.60	30.98
Middle-reflector + 3-step	14.5	12.75	12.25	15.50	3.110	12.265	82.92	31.64
Matched	14.5	12.50	12.50	15.50	3.110	12.500	80.62	31.36

Table.S3
PV performance parameters of devices measured in Fraunhofer ISE and EPFL.

Cell number	Measured in -	V_{OC} (V)	FF (%)	J_{SC} (mA/cm^2)	PCE (%)
3052-8	Fraunhofer ISE	3.12	81.80	11.46	29.28
3052-8	EPFL	3.02	81.27	12.10	29.80
3052-9	Fraunhofer ISE	3.09	82.97	11.29	28.96
3052-9	EPFL	3.03	82.79	12.03	30.23
3054-1	Fraunhofer ISE	3.10	82.40	11.12	28.45
3054-1	EPFL	3.03	82.81	11.60	29.07
3054-5	Fraunhofer ISE	3.05	78.53	11.47	27.46
3054-5	EPFL	3.03	81.31	12.00	29.55
3054-6	Fraunhofer ISE	3.13	80.32	10.98	27.60
3054-6	EPFL	2.99	81.62	11.67	28.47
3054-7	Fraunhofer ISE	3.10	81.90	11.42	29.00
3054-7	EPFL	3.04	81.69	11.94	29.60
3061-2	Fraunhofer ISE	3.07	83.06	11.11	28.35
3061-2	EPFL	3.02	83.62	11.70	29.53
3061-6	Fraunhofer ISE	3.13	78.46	11.49	28.27
3061-6	EPFL	3.06	83.24	11.71	29.86
3061-9	Fraunhofer ISE	3.11	81.52	11.30	28.67
3061-9	EPFL	3.06	83.24	11.71	28.86
3115-8	Fraunhofer ISE	3.12	83.26	11.03	28.67
3115-8	EPFL	3.05	83.70	11.58	29.07

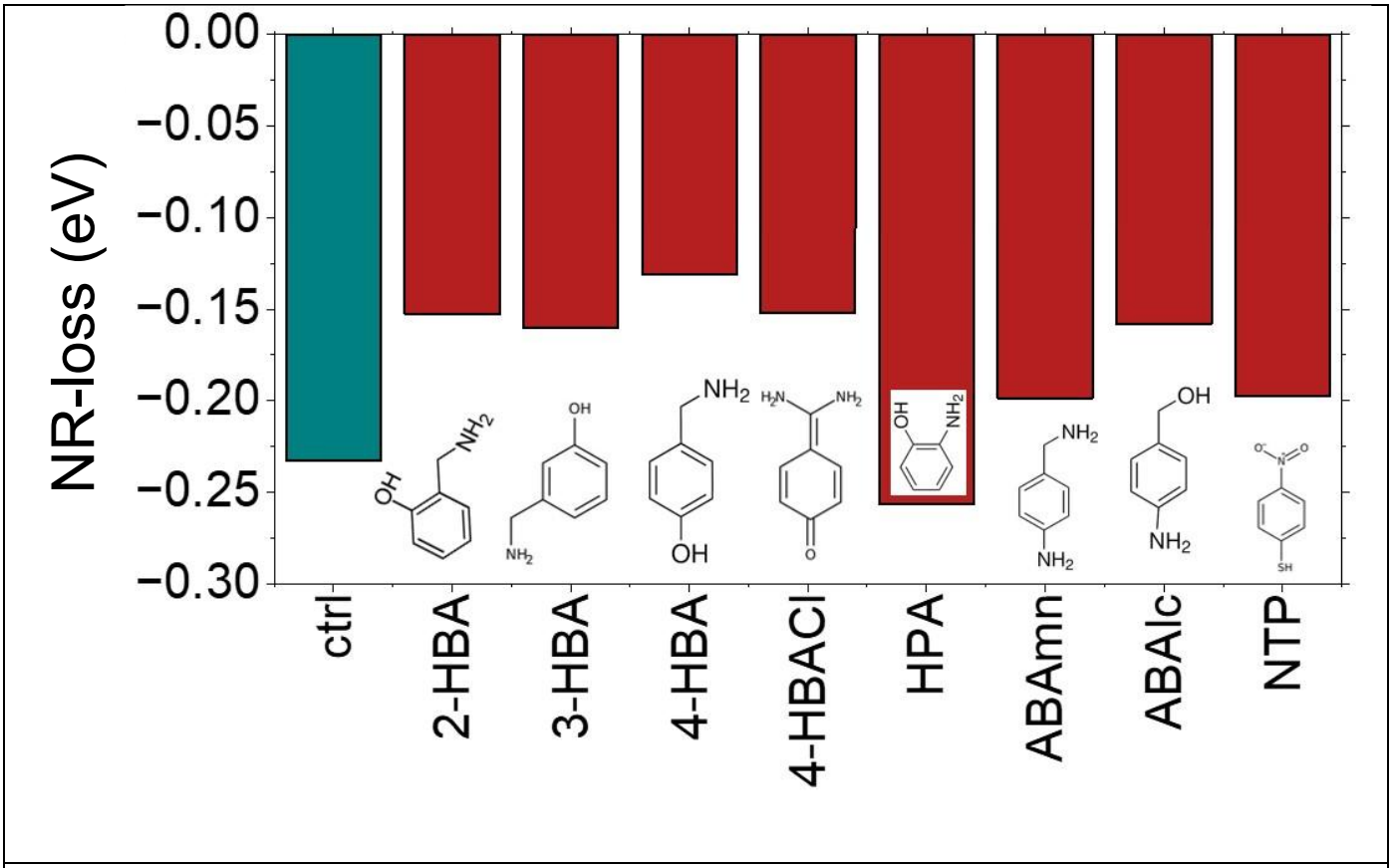

Figure S1. Non-radiative losses of the stack ITO/Me-4PACz/SiOx-np(0.1%)/perovskite with different additives.

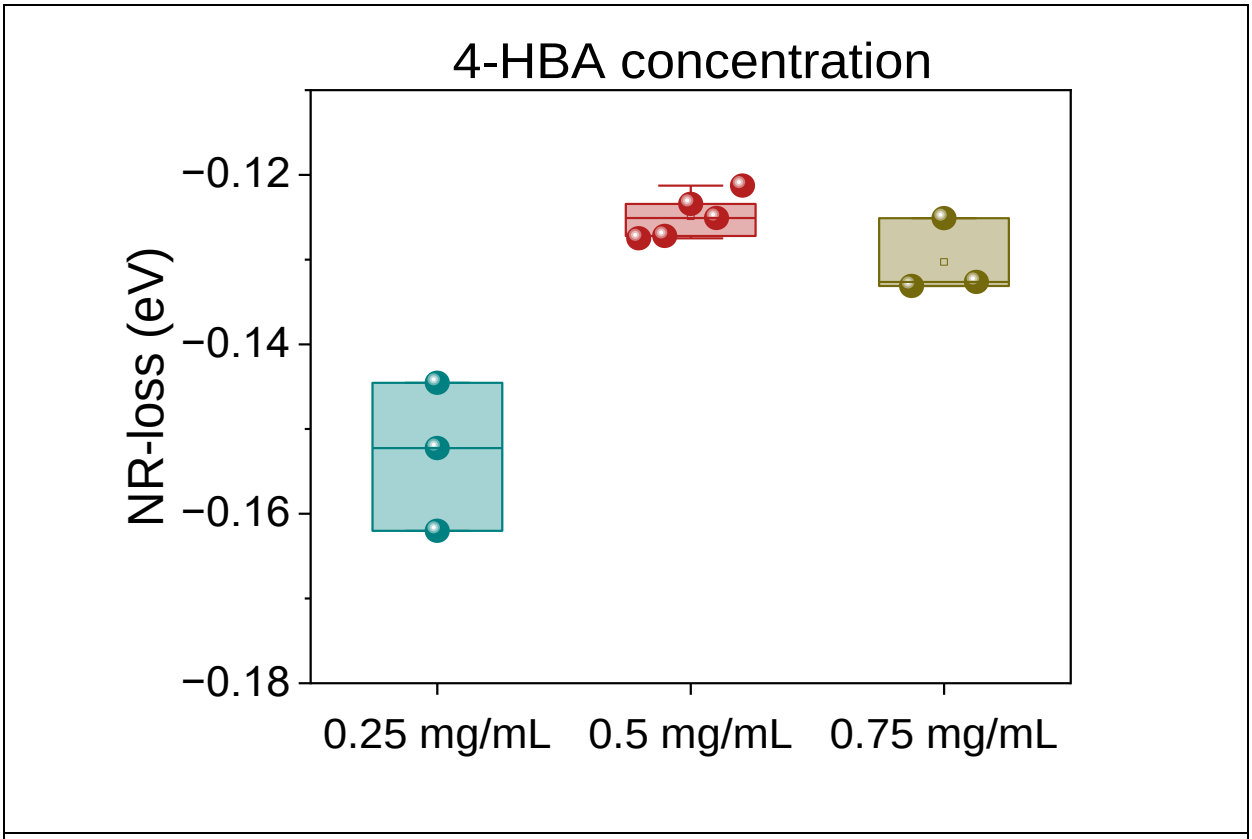

Figure S2. HBA-concentration optimization on half-cell stacks, ITO/**Me-4PACz/SiOx-np(0.1%)**/perovskite.

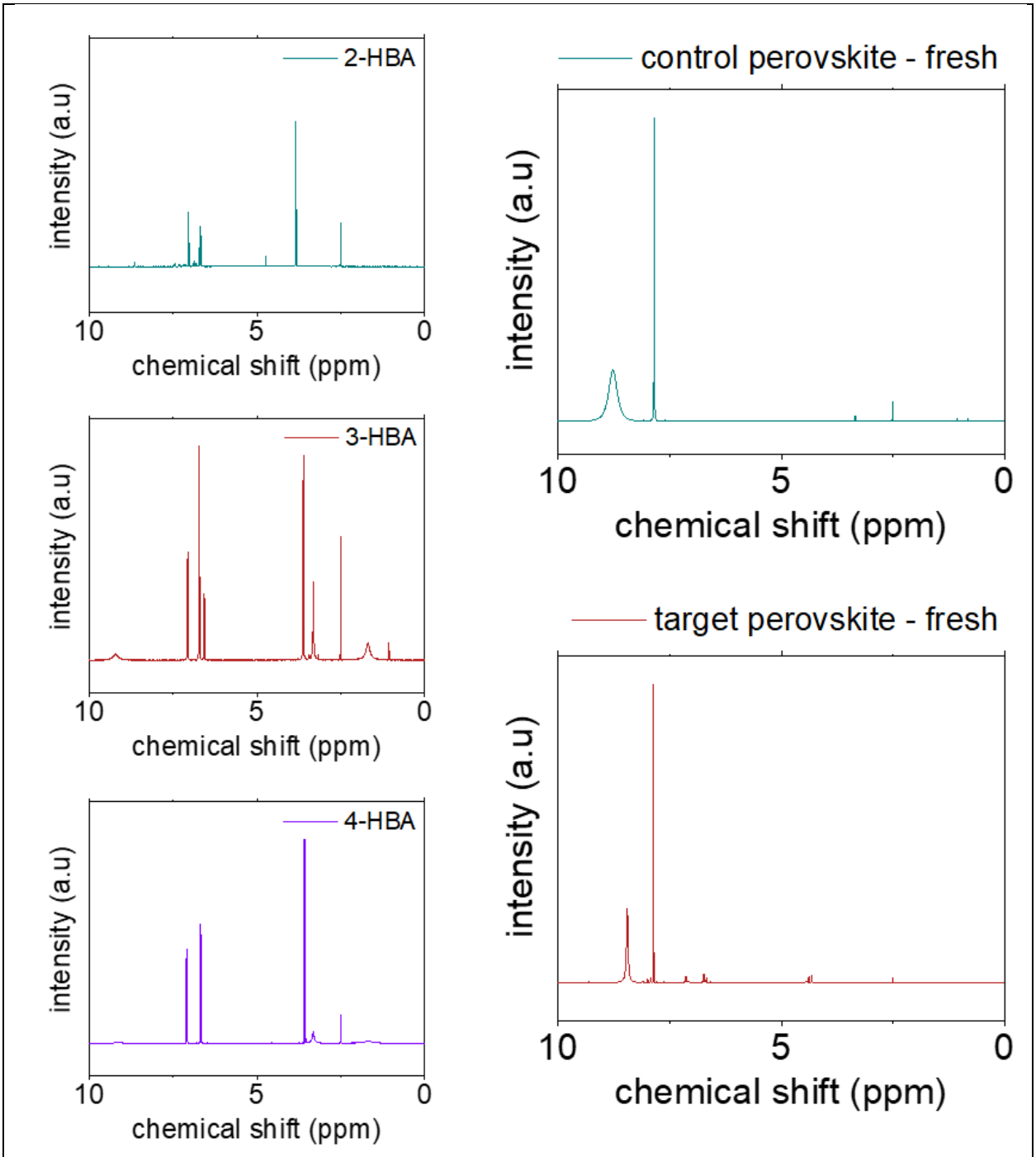

Figure S3. NMR spectra of HBA-derivatives, control and target perovskite (fresh).

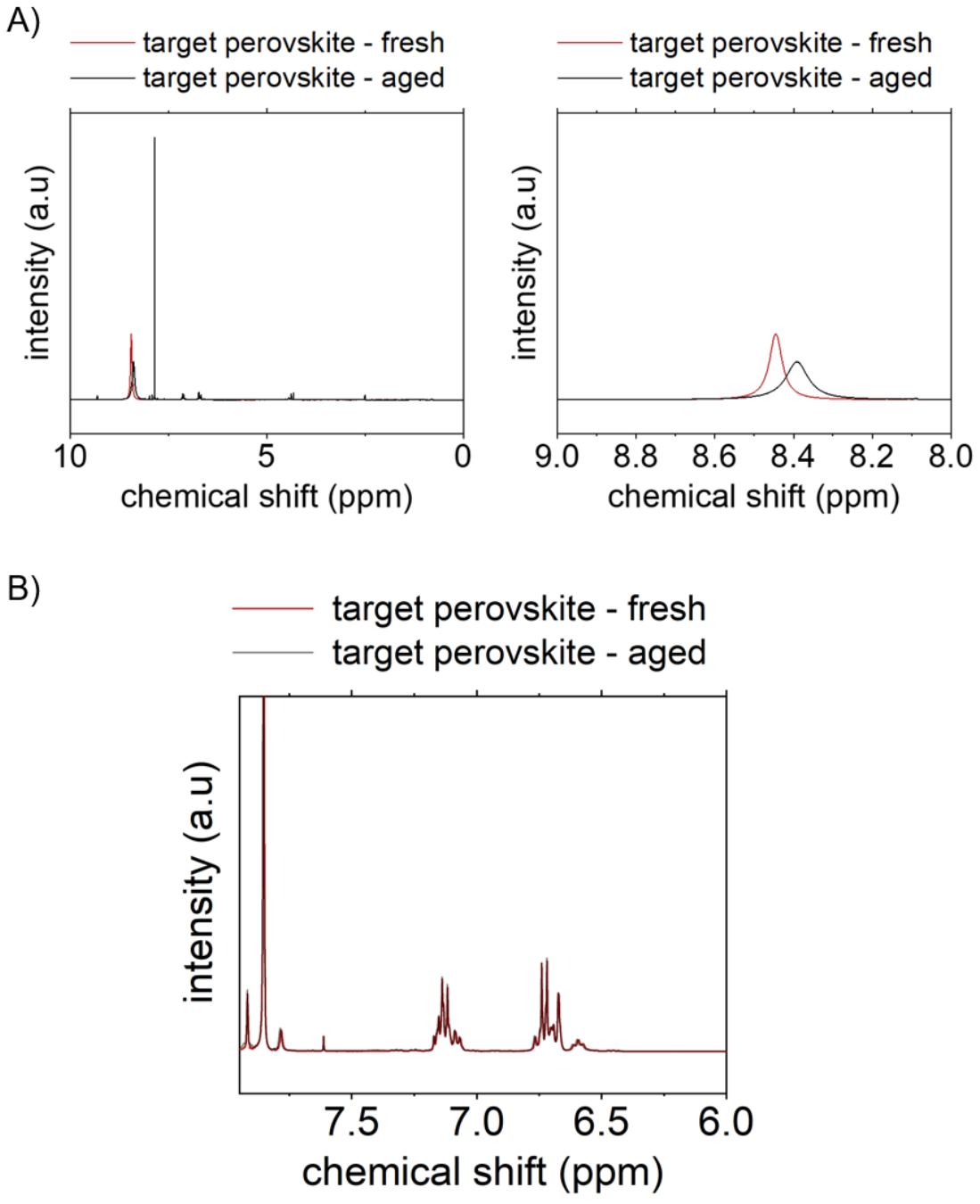

Figure S4. A) NMR spectrum of target perovskite (fresh and aged). Second graph with zoom-in to the peak at 8.45 ppm (-NH_2 of FAI). B) NMR spectrum of target perovskite (fresh and aged), highlighting perfect overlap in the non-exchangeable aromatic peaks of HBAs.

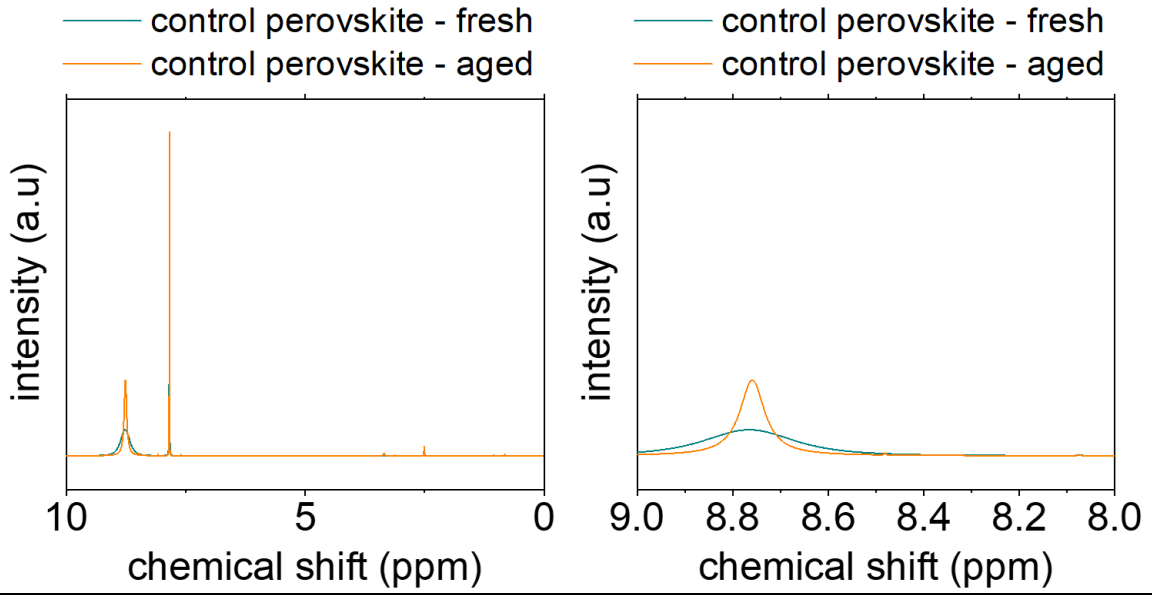

Figure S5. NMR spectrum of the control perovskite (fresh and aged). Second graph with zoom-in to the peak at 8.75 ppm (-NH_2 of FAI).

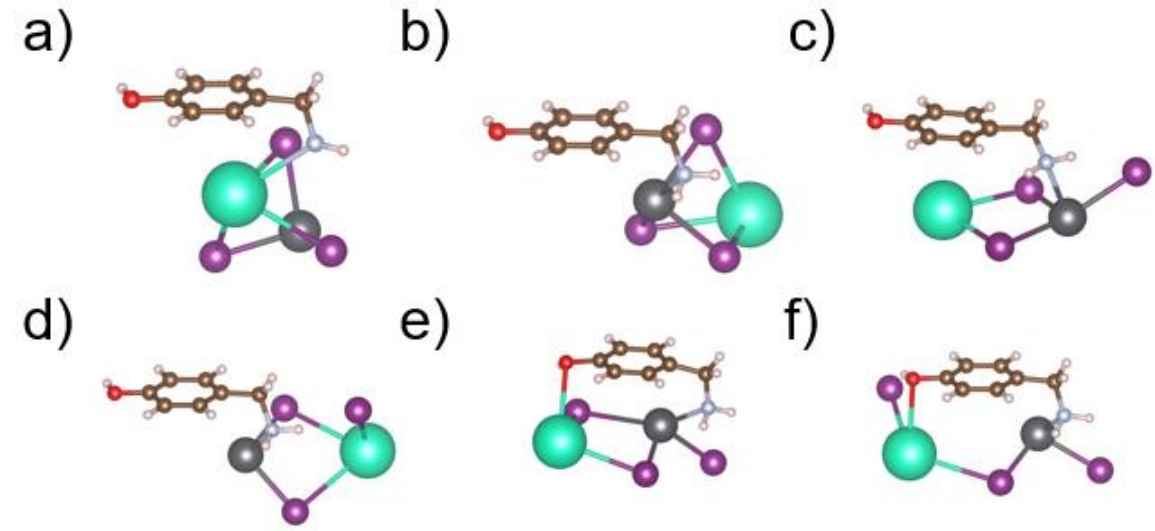

Figure S6. (a)-(c) Interaction of 2-3-4- HBA with a FA cation. (d)-(f) Interaction of 2-3-4-HBA with the model perovskite $CsPbI_3$. Binding energies calculated with DFT are given in **Table.S2**. Carbon atoms are shown as brown spheres, hydrogen as white, nitrogen as blue, oxygen as red, lead as black, and cesium as green (*19*).

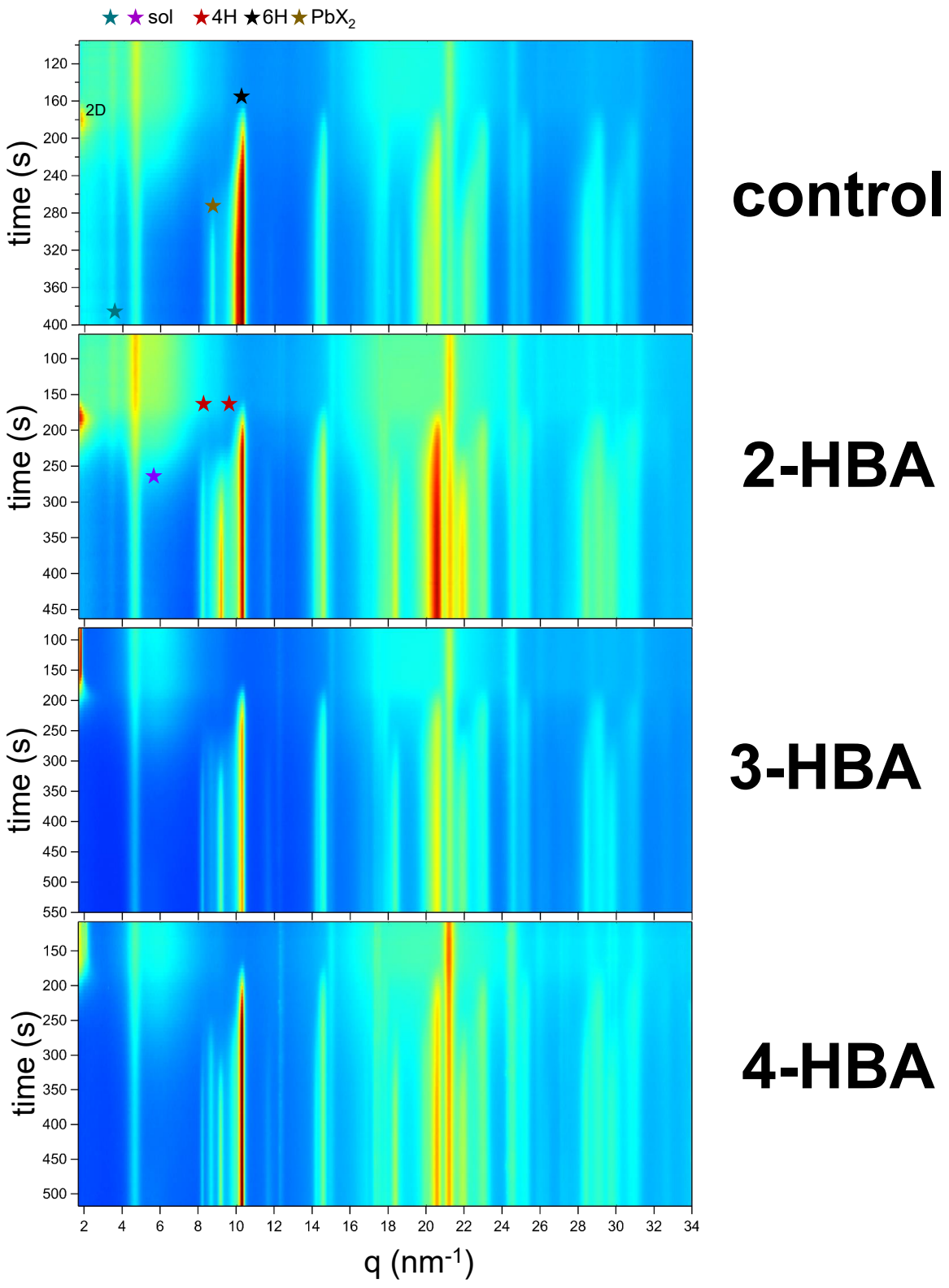

Figure S7. In-situ GIWAXS measurements during spinning.

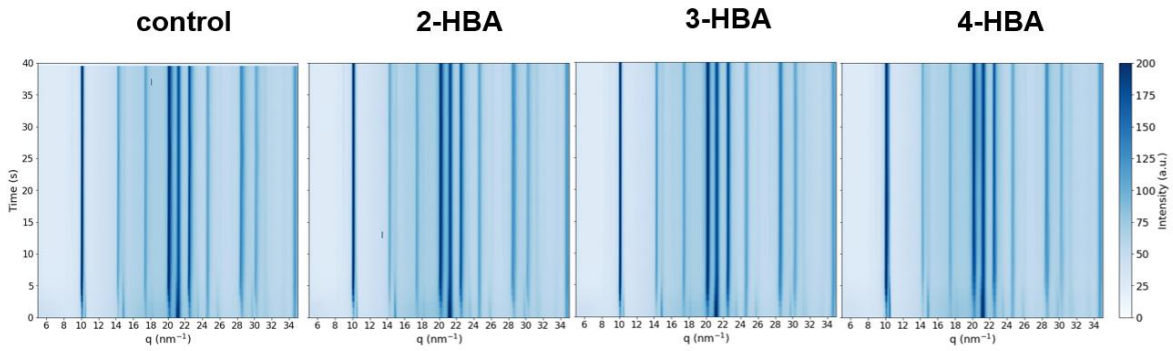

Figure S8. In-situ GIWAXS measurements during annealing.

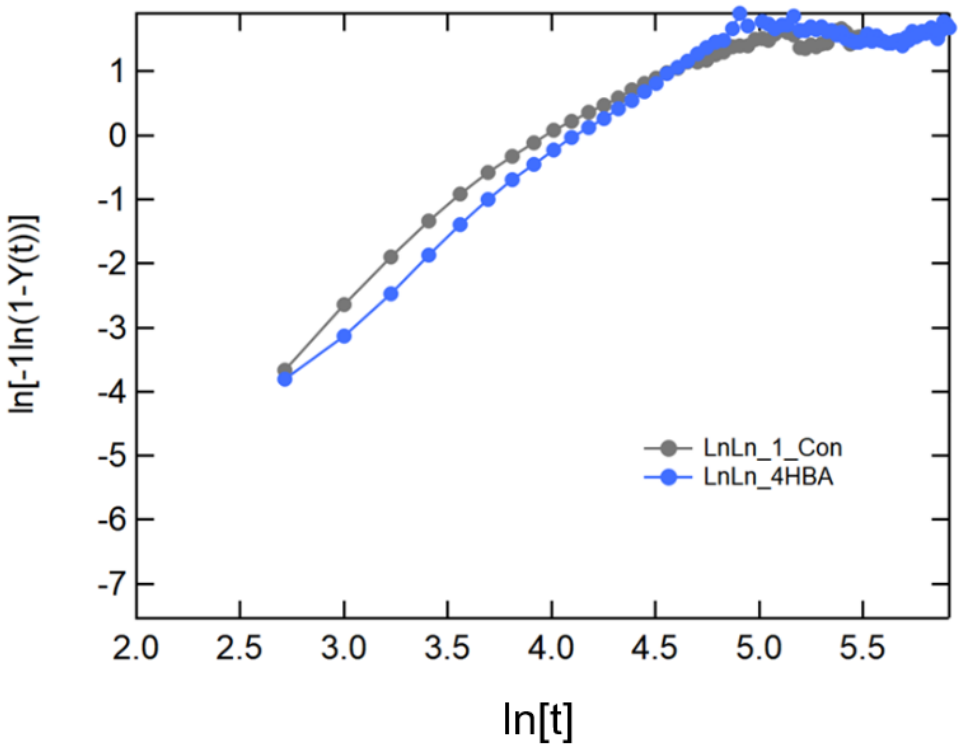

Figure S9. Avrami plots for control and 4-HBA extracted from **in-situ annealing** experiment.

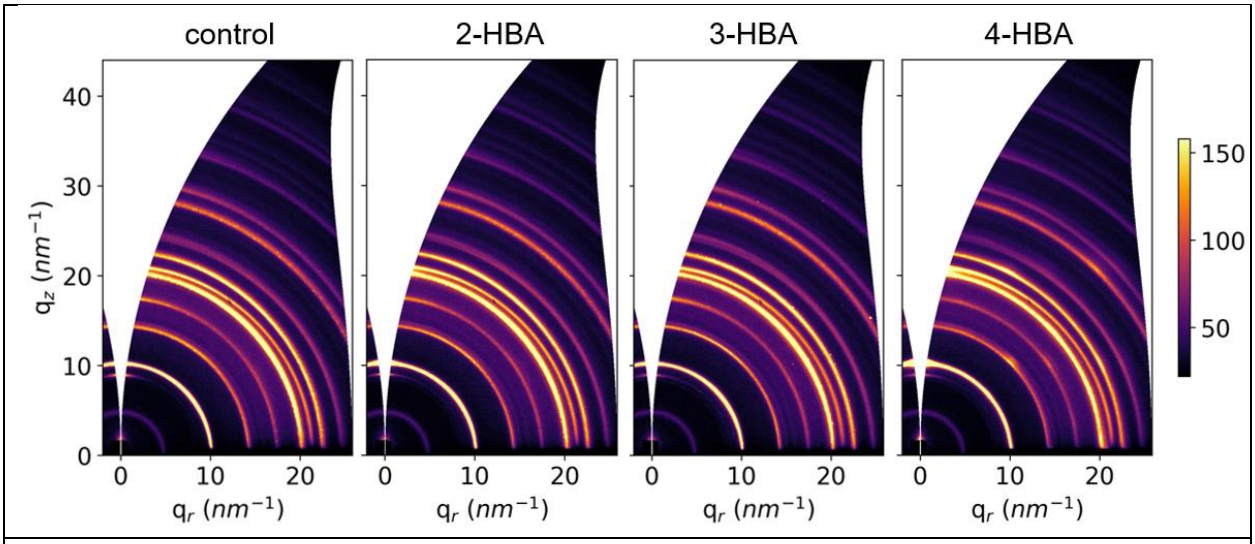

Figure S10. Ex-situ GIWAXS measurements after film formation.

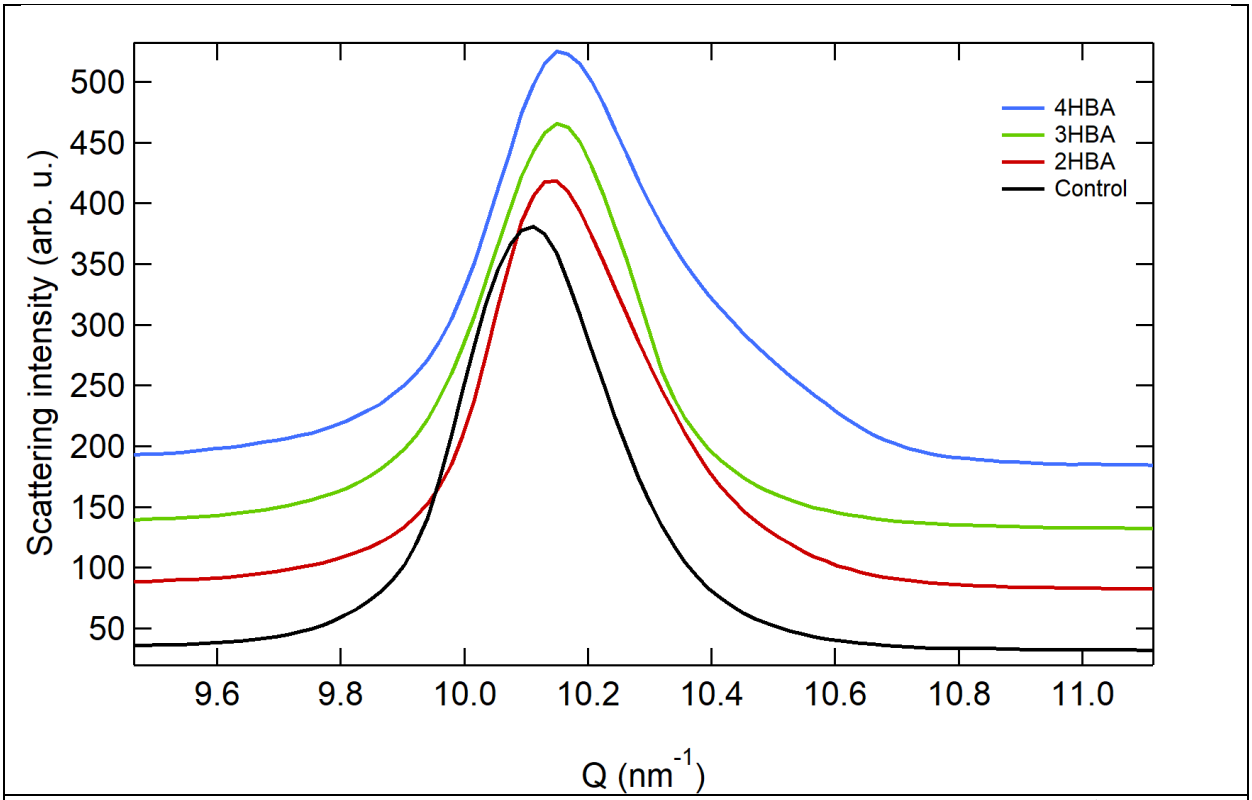

Figure S11. Ex-situ GIWAXS measurements, shift in the main perovskite peak at 10.1 nm^{-1}, indicates reduced unit cell volume.

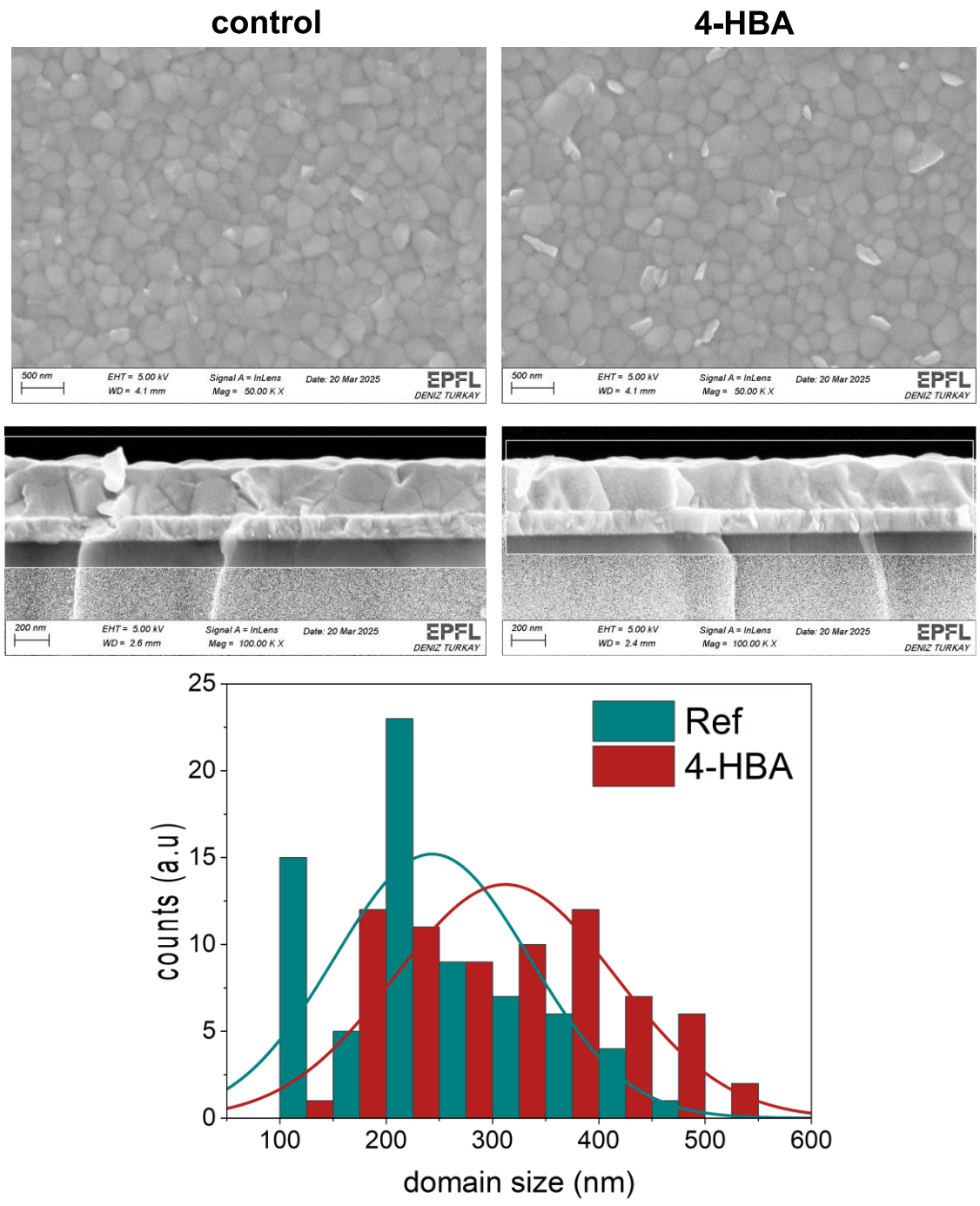

Figure S12. Top-view and cross-section SEM of ITO/perovskite samples, with and without 4-HBA additive. Domain size analysis from the top-view SEM.

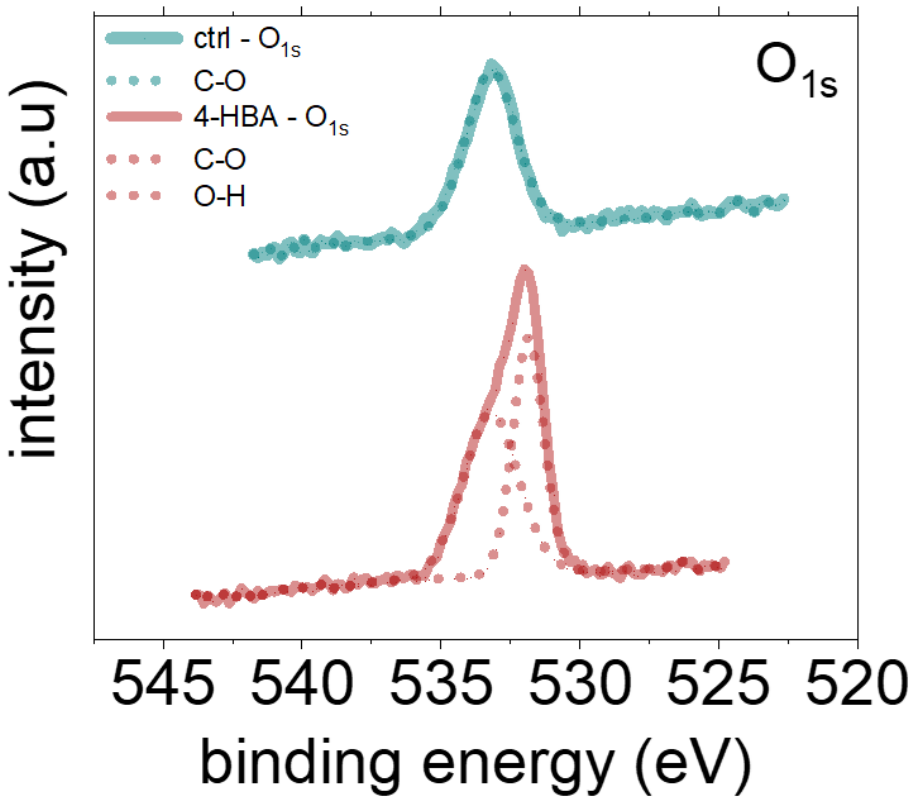

Figure S13. O_{1s} XPS spectrum of control and 4-HBA devices, the origin of C-O contribution is attained to atmospheric contamination.

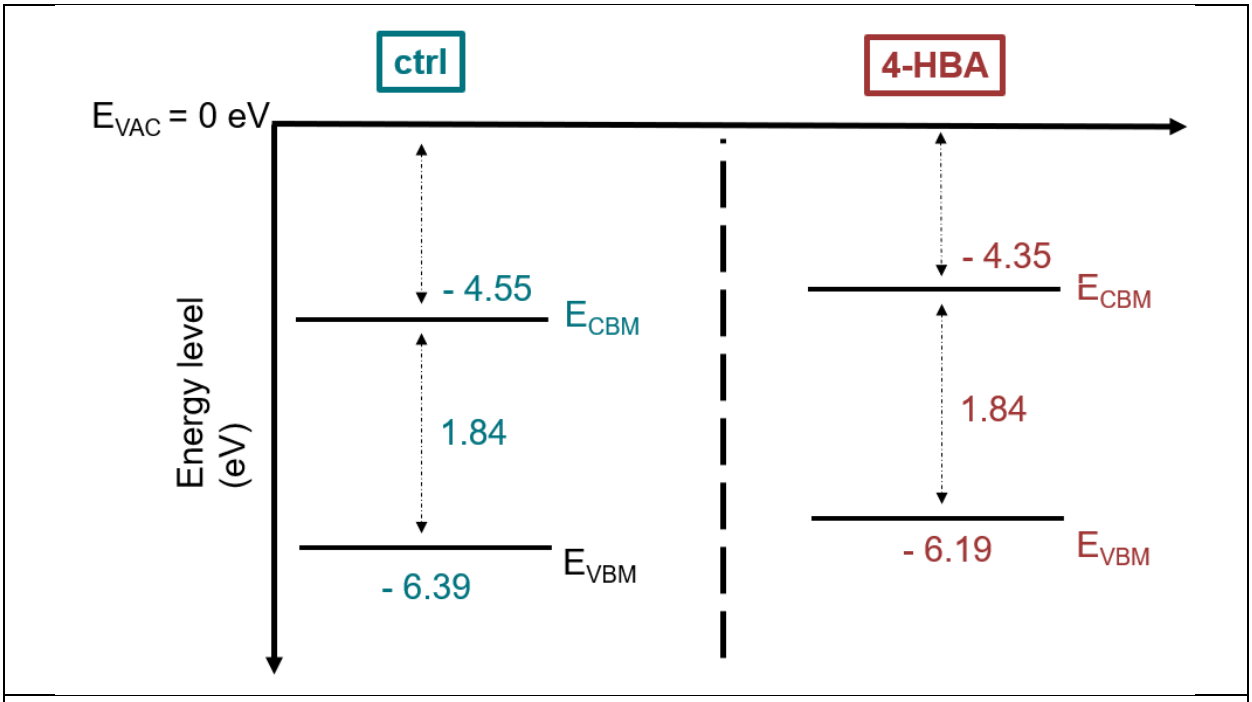

Figure S14. Changes in the band energetics with the 4-HBA additive.

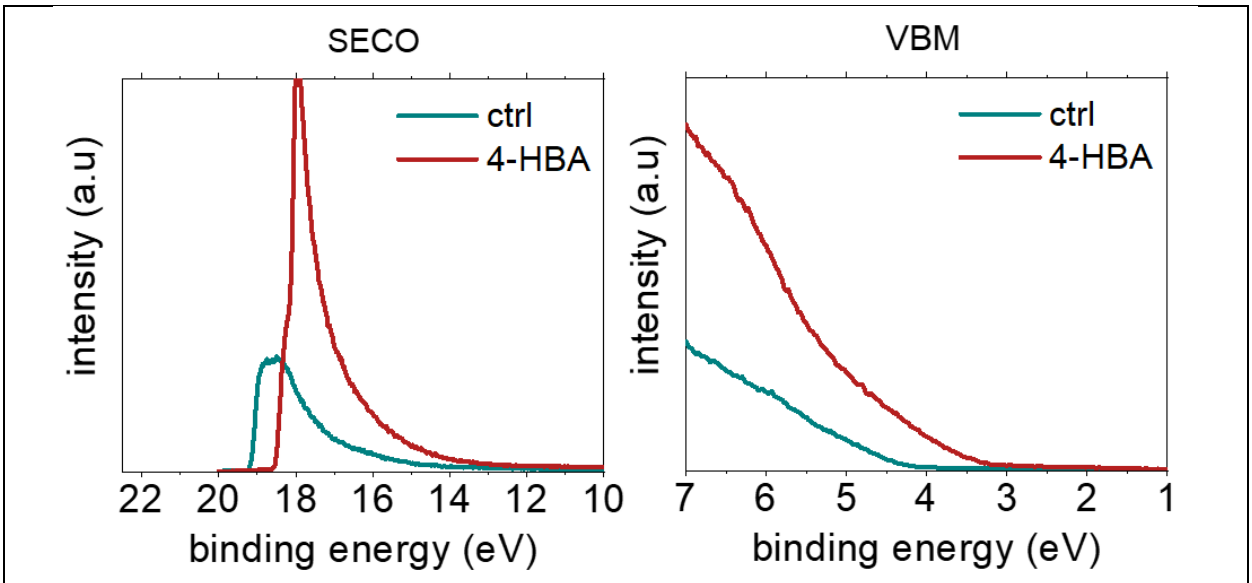

Figure S15. SECO and VBM of control and 4-HBA devices.

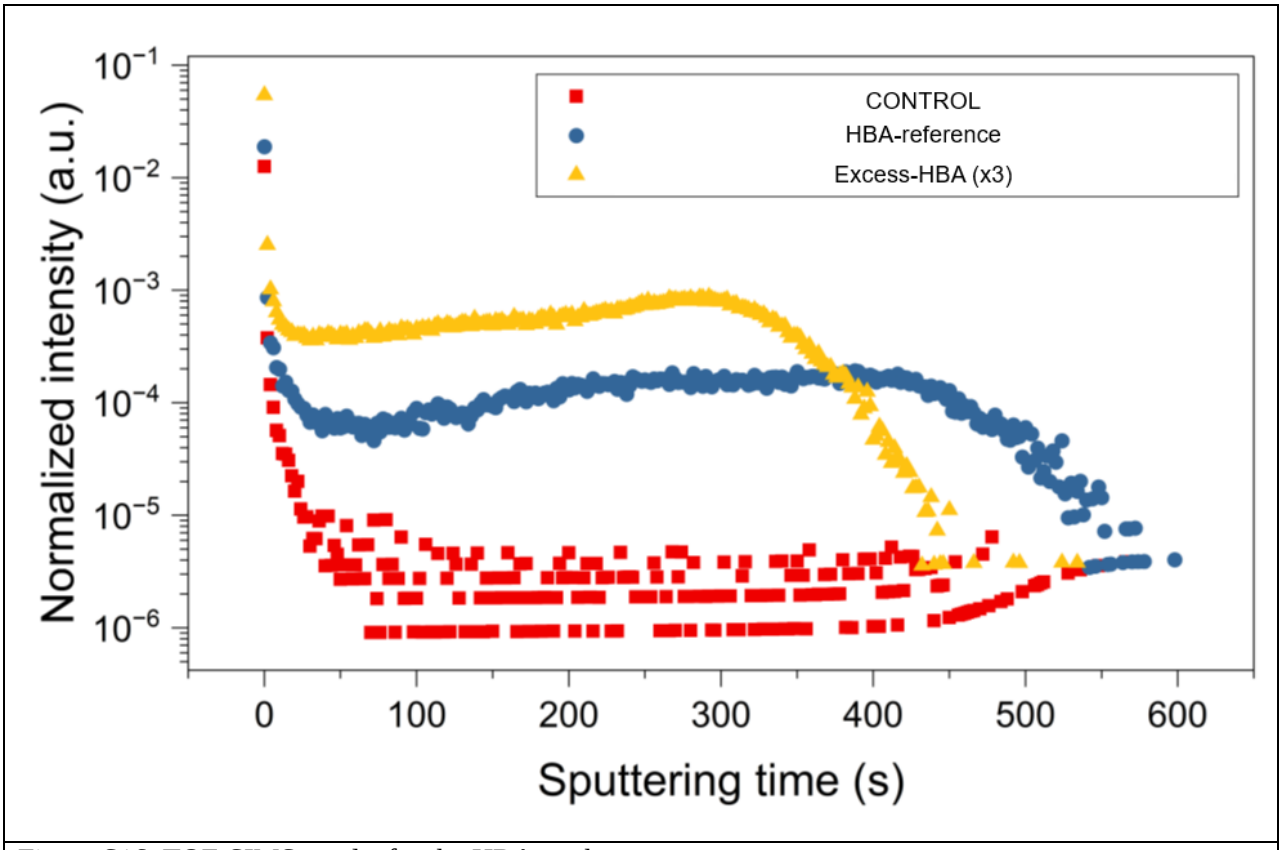

Figure S16. TOF-SIMS results for the HBA-peak.

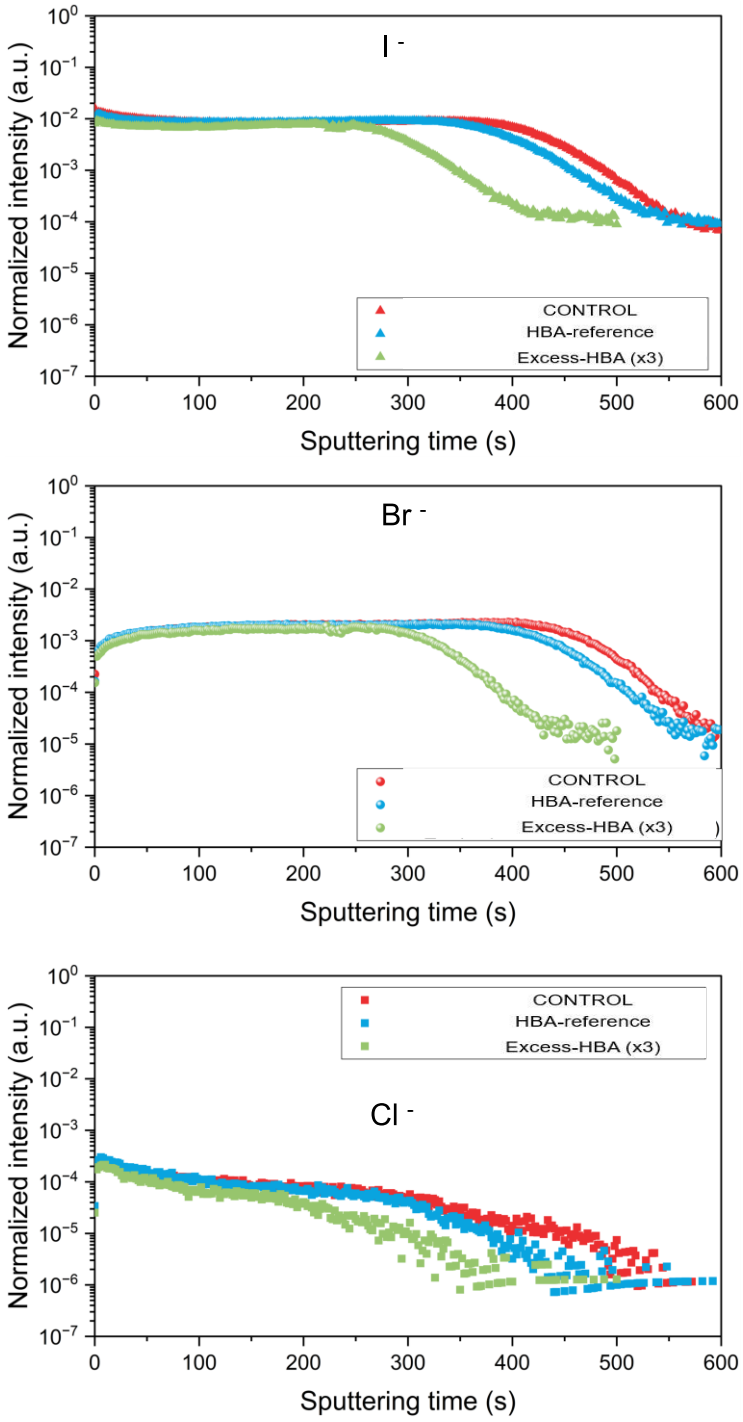

Figure S17. TOF-SIMS results for different halides. The faster fading of the signal with increasing HBA concentration is a result of dilution of the perovskite ink (and hence lower film thickness).

(a)

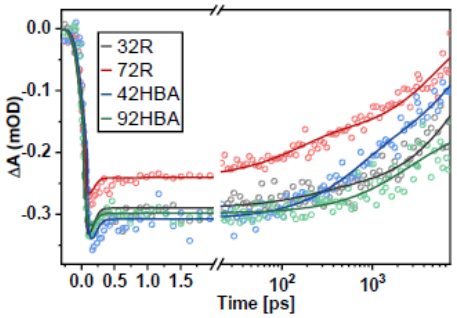

(b)

Sample	τ_1 [ps]	τ_2 [ps]	τ_3 [ns] *
32R	< 0.15 ps	205 ± 121	11.5 ± 1.2
72R	< 0.15 ps	141 ± 33	5.4 ± 0.5
42HBA	< 0.15 ps	612 ± 146	8.9 ± 1.4
92HBA	< 0.15 ps	1862 ± 1426	46 ± 96

Figure S18. a) Transient absorption kinetic traces extracted from the ground state bleach minima at 678 nm for the different samples. b) Lifetimes extracted from a three-exponential decay function. We observe the trend of longer lifetimes for HBA samples.

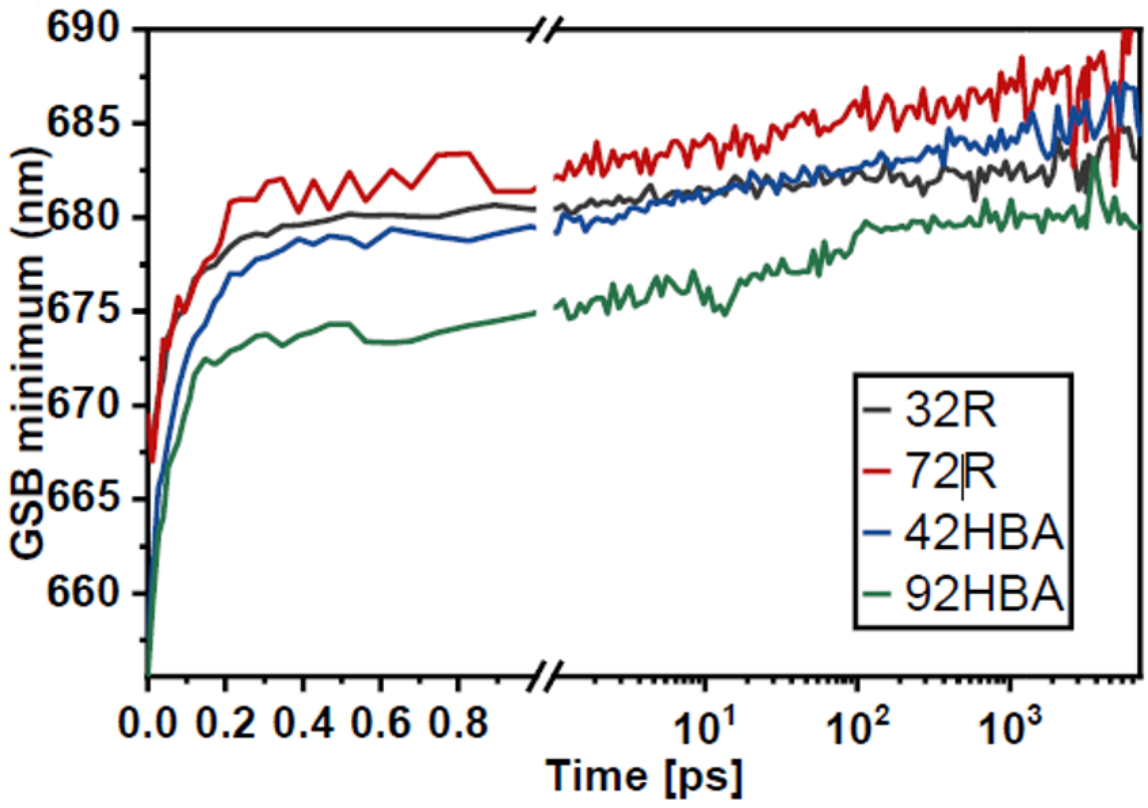

Figure S19. The wavelength position of the minimum of the ground state bleach as a function of delay time is shown, obtained from fitting a Gaussian function to the transient spectrum at every delay time after zero. In the first 400 fs, we can observe charge carrier thermalization, while at longer delay times, the shift may arise from phase segregation. The phase segregation is less pronounced in HBA samples.

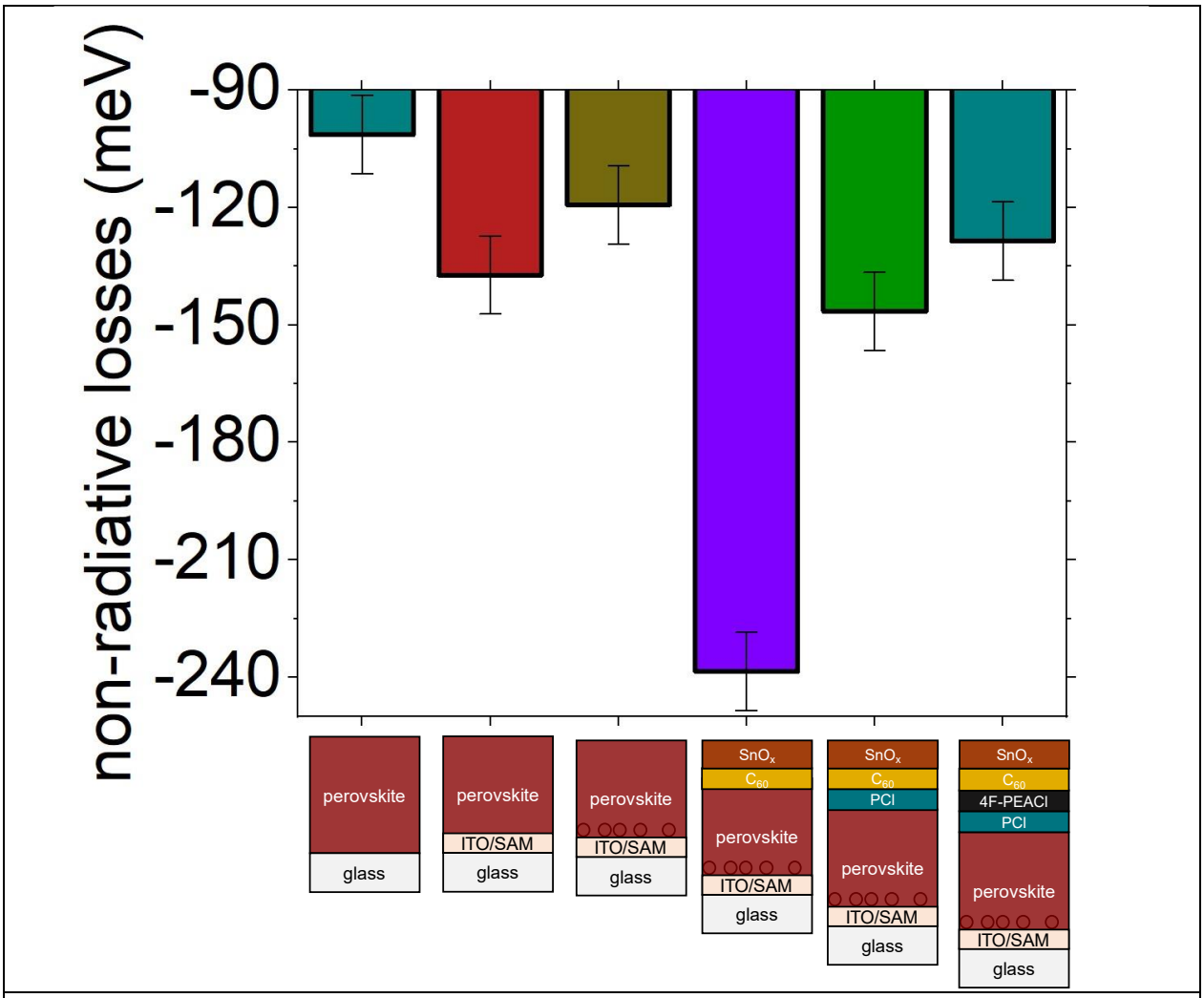

Figure S20. Non-radiative loss analysis of WBG top cells

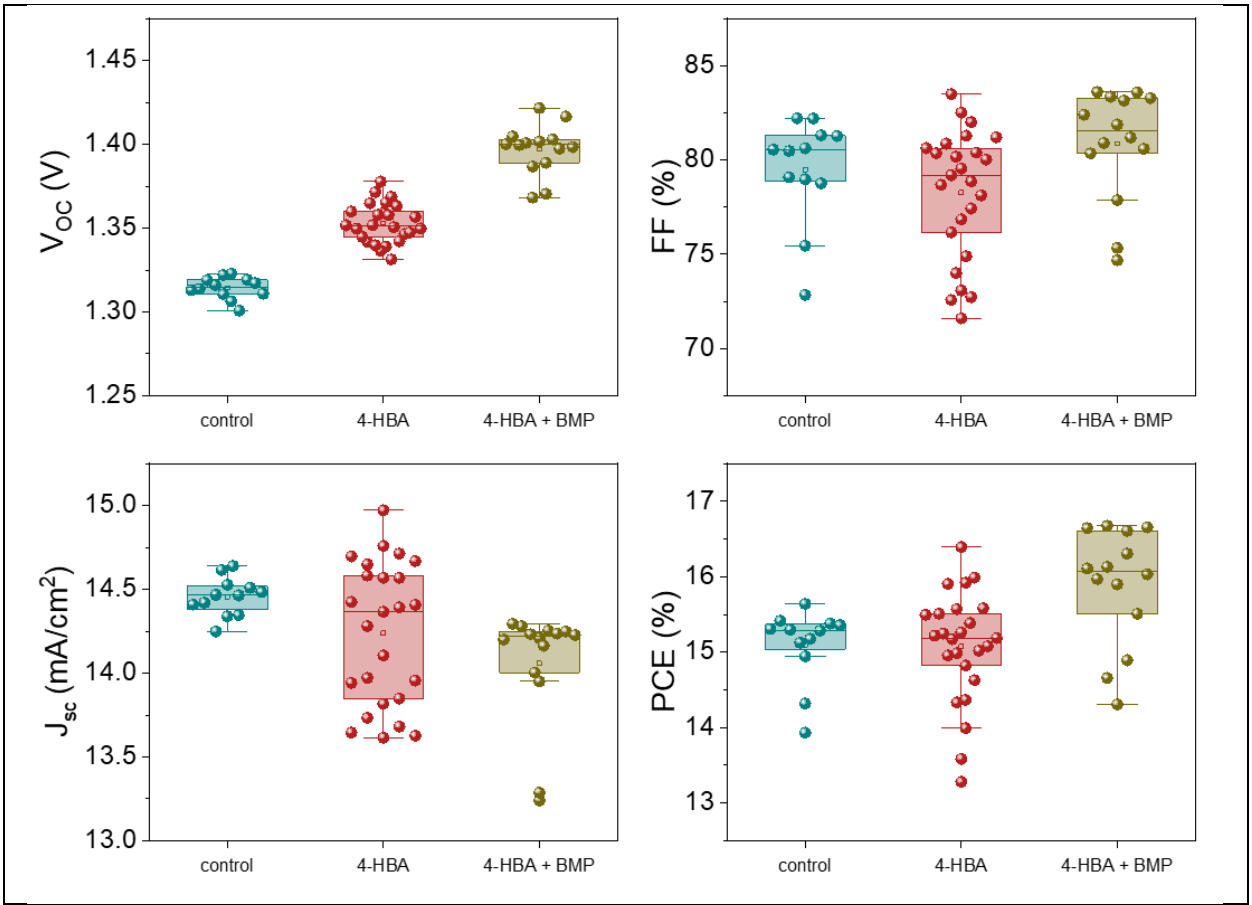

Figure S21. PV performance parameters of WBG single junction devices (control, 4-HBA and 4-HBA with bimolecular passivation - BMP).

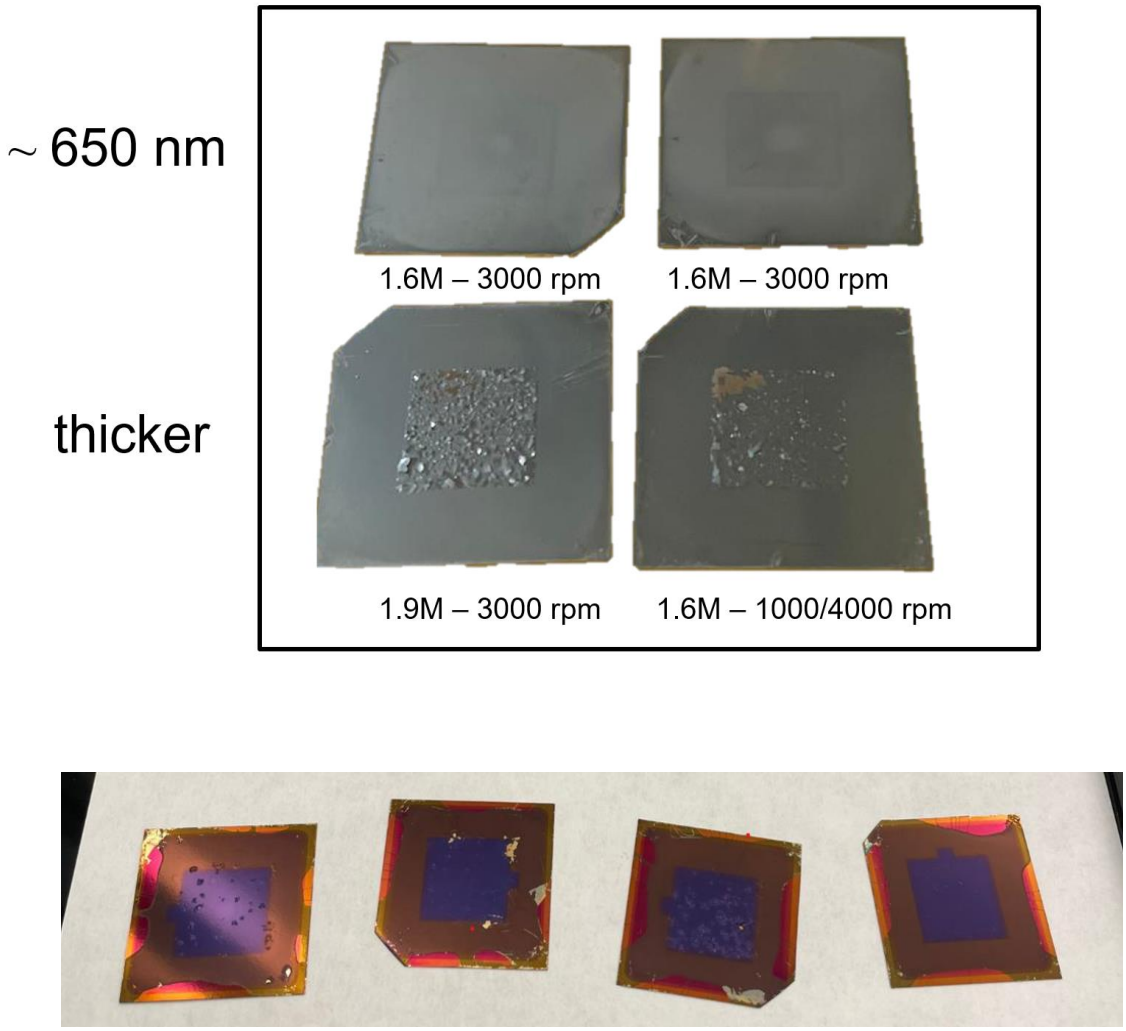

Figure S22. Top row: peeling off (delamination from the HTL side) during passivation processing, just before adding the C_{60} on the thick MBG absorber. Bottom row: Peeling off during top-cell SAM processing.

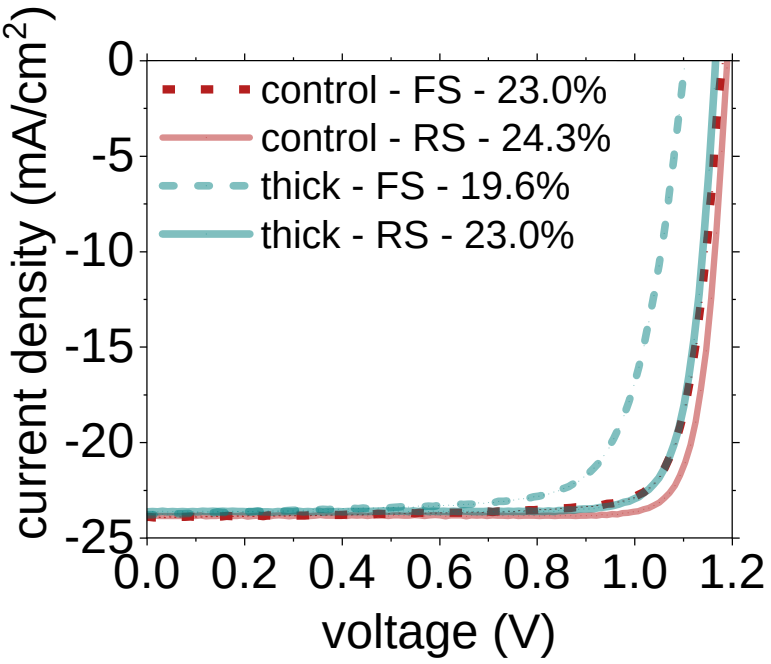

Figure S23. JV results of the champion thin and thick MBG cells on 2PACz:4PADCB HTLs. Delamination is not observed.

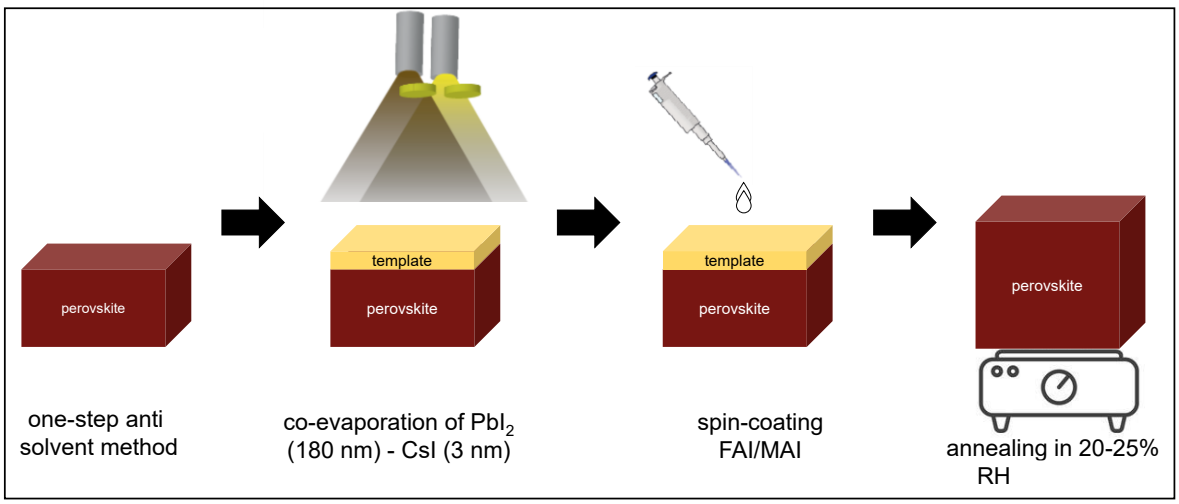

Figure S24. Fabrication procedure of three-step absorbers.

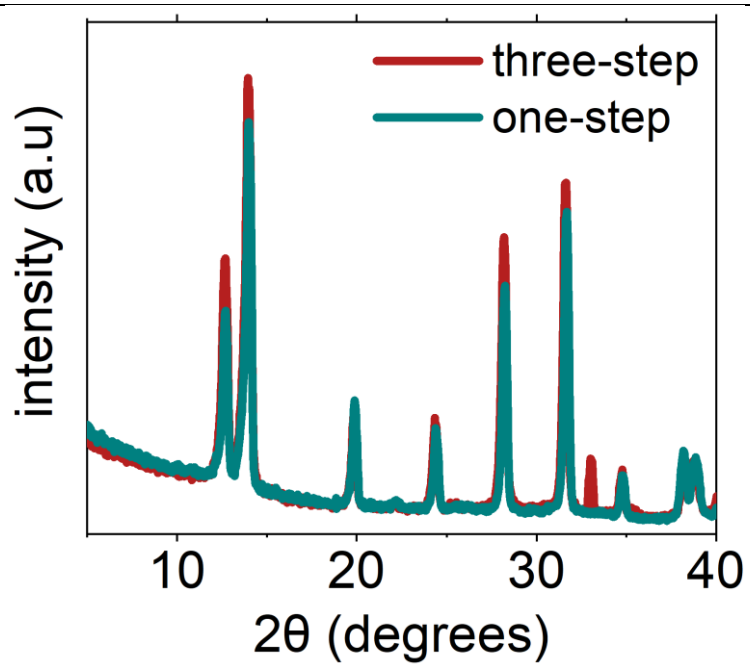

Figure S25. XRD of one-step and three-step absorbers.

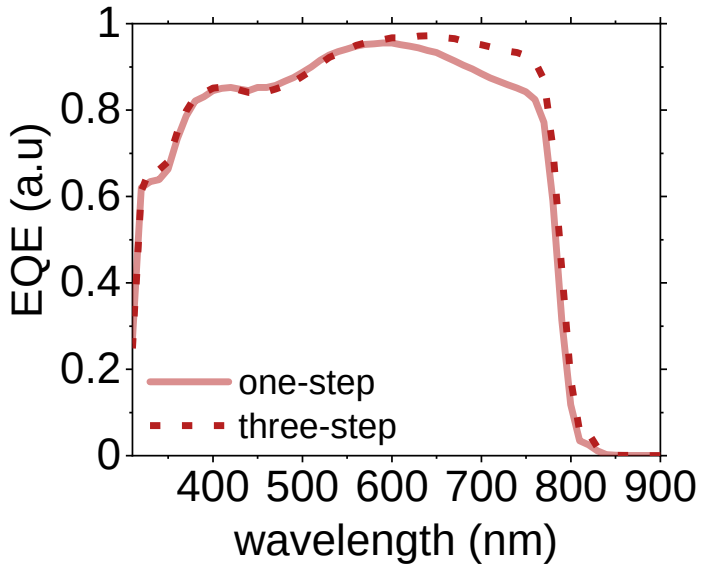

Figure S26. EQE comparison of one and three-step absorber on ohmic-Si substrates.

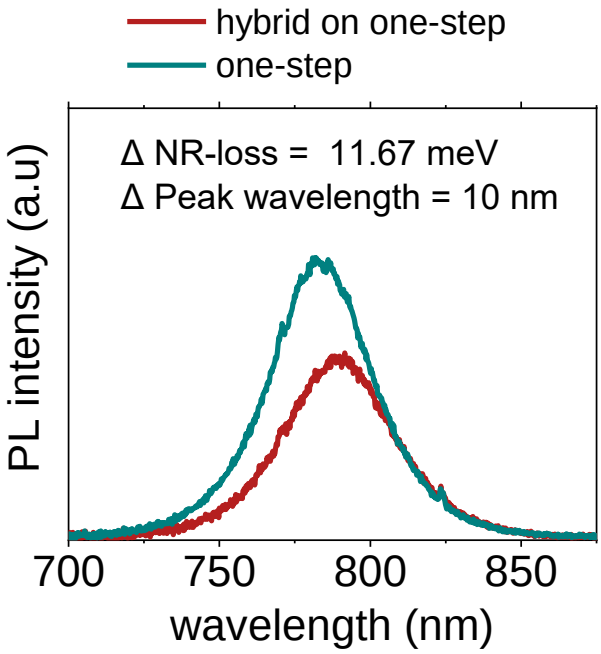

Figure S27. PLQY spectrum of the one-step and three-step absorbers.

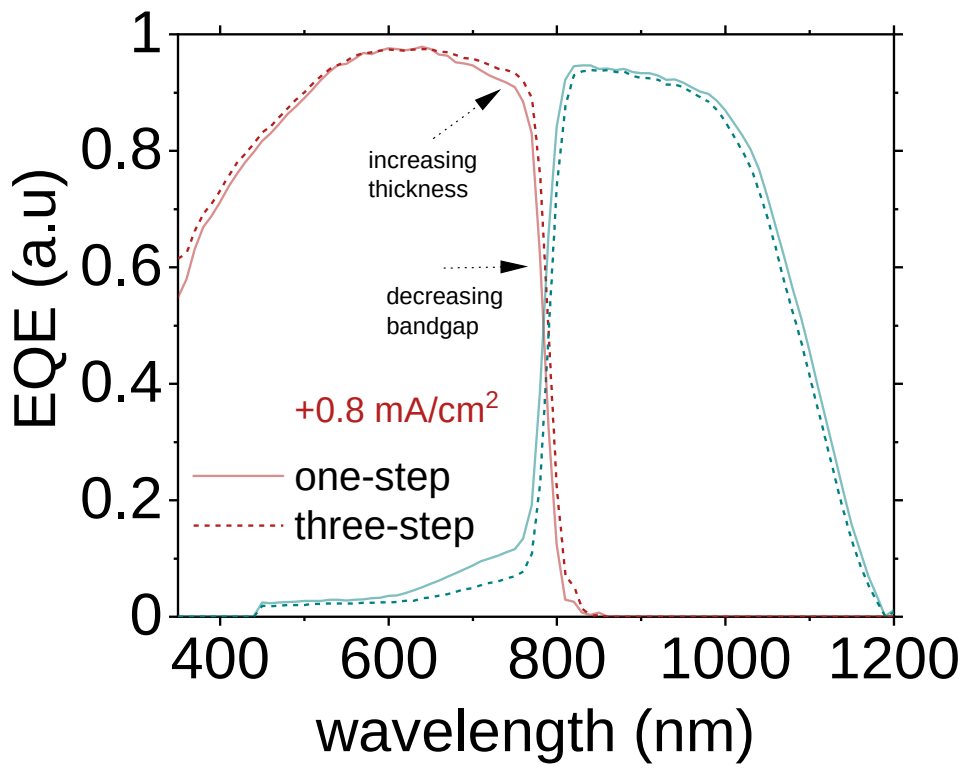

Figure S28. EQE of MBG-Si tandems with one-step and three-step (hybrid on one-step) absorbers.

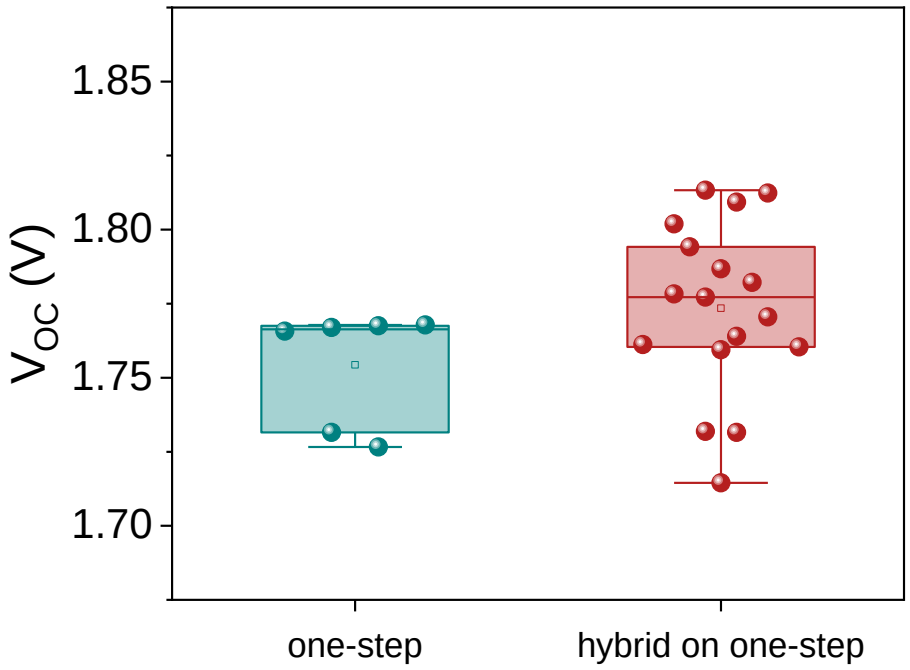

Figure S29. V_{OC} of MBG-Si tandems with one-step and hybrid on one-step absorbers.

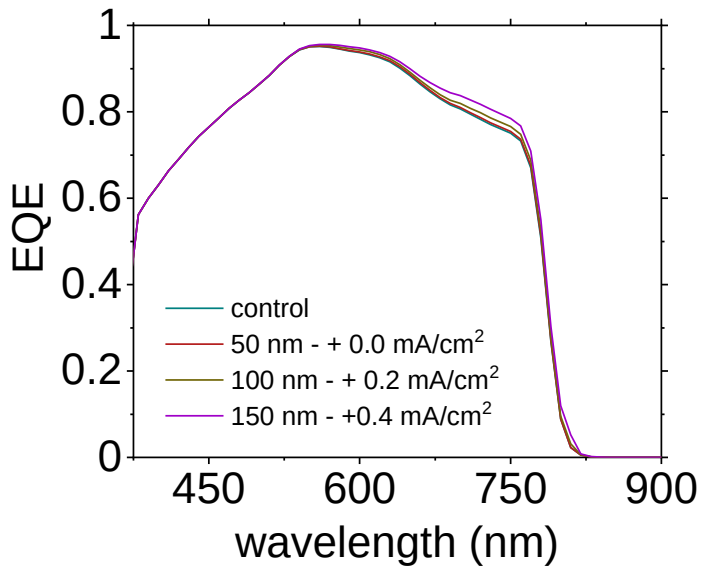

Figure S30. COMSOL simulation results for middle-reflector with different filling ratios.

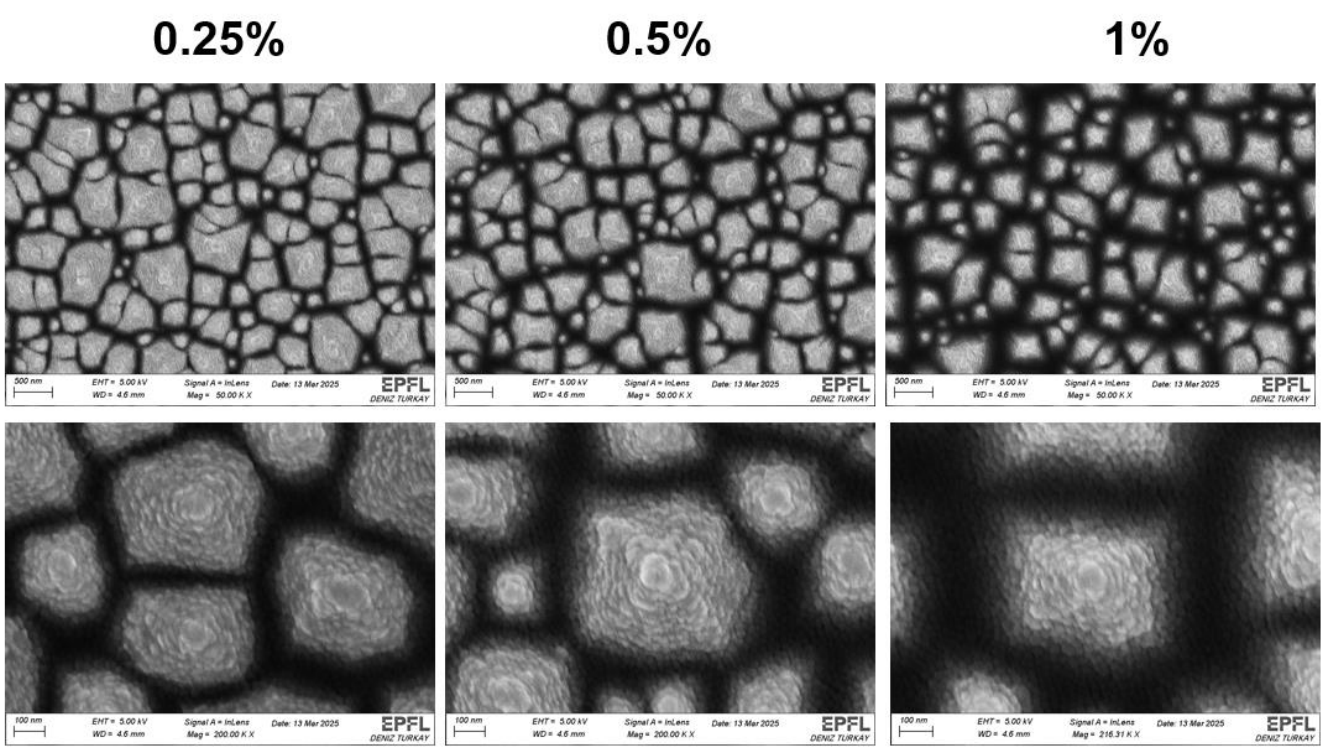

Figure S31. Top-view SEM images of different concentrations of middle-reflector (SiOx-np) on textured c-Si substrates.

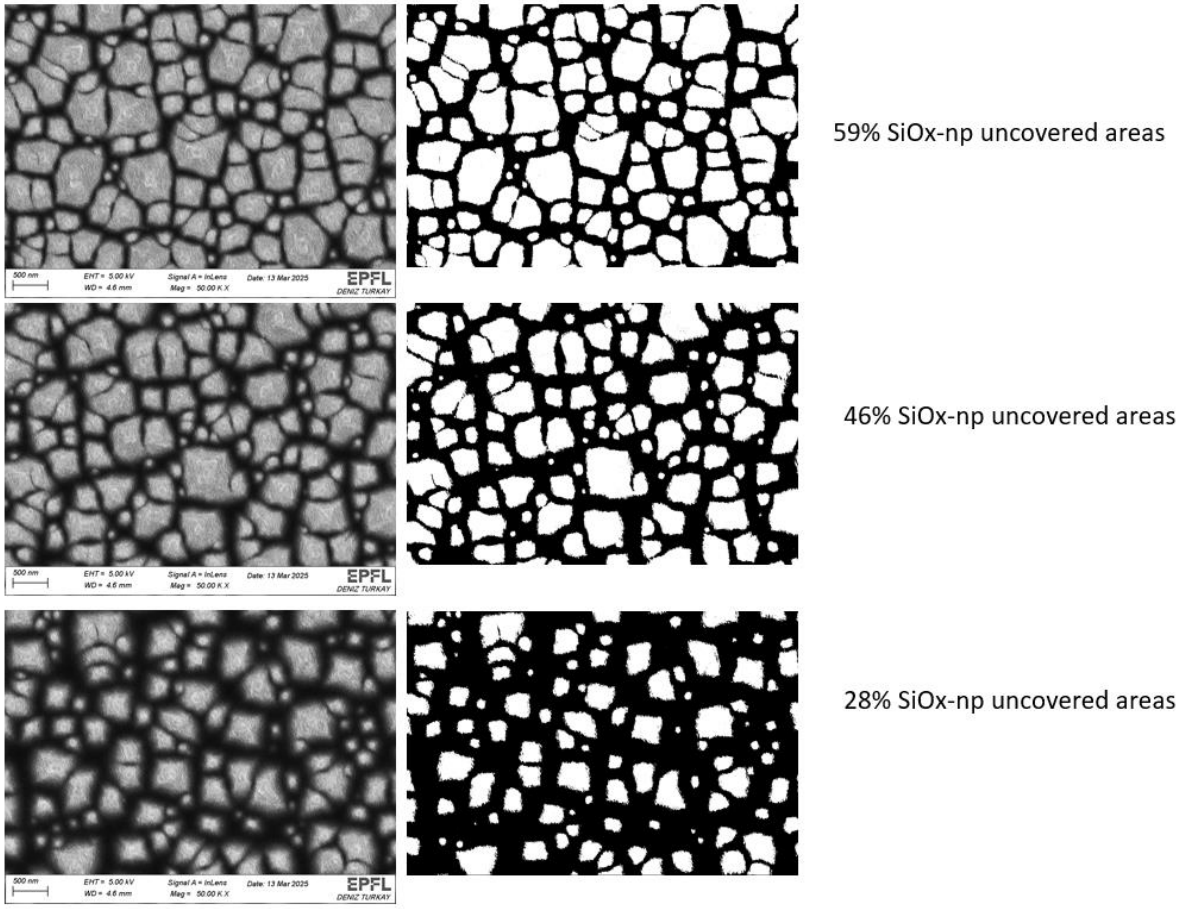

Figure S32. Image analysis of different concentrations of middle-reflector to quantify the SiO_x-np uncovered areas. Filling height (h) is calculated from the percentage of uncovered areas. The height of the pyramid tip (H) is taken as 260 nm.

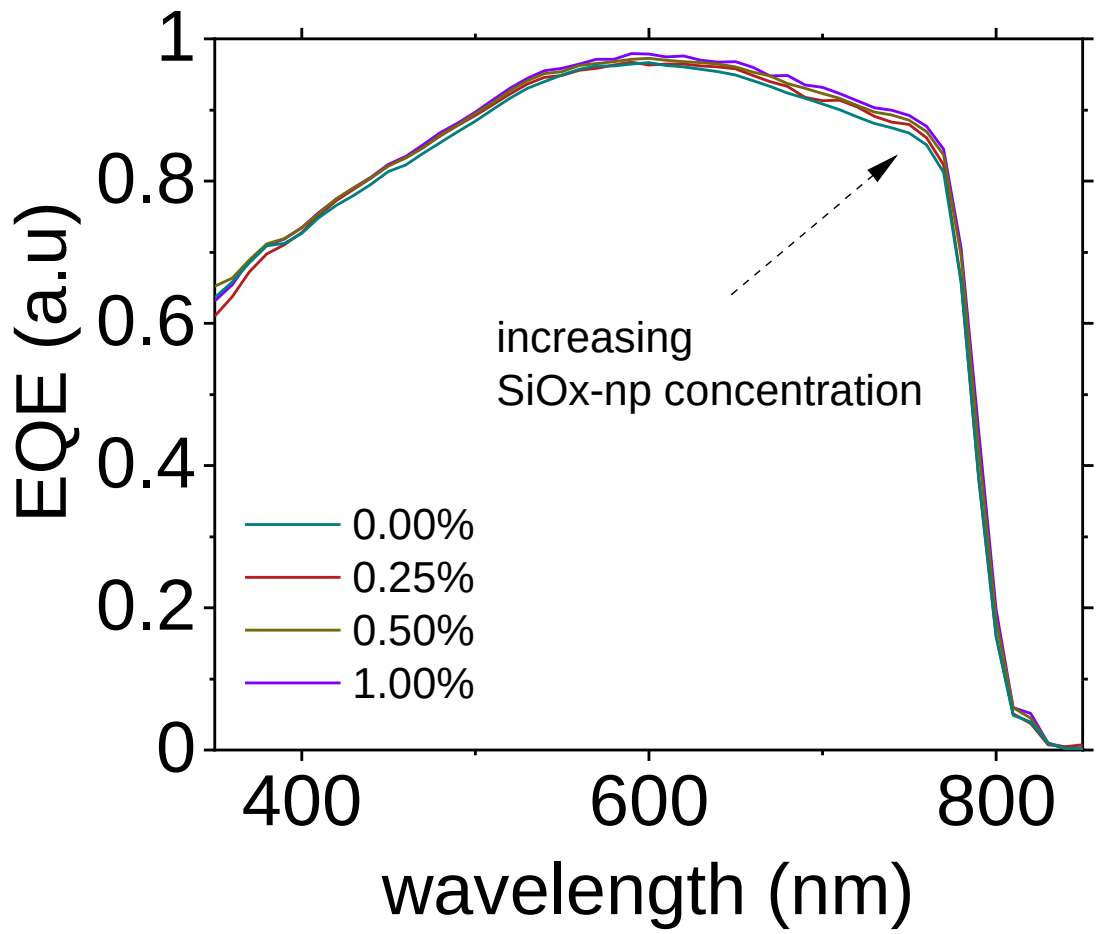

Figure S33. MBG cell EQE results for MBG-Si tandems with different concentrations of middle-reflector.

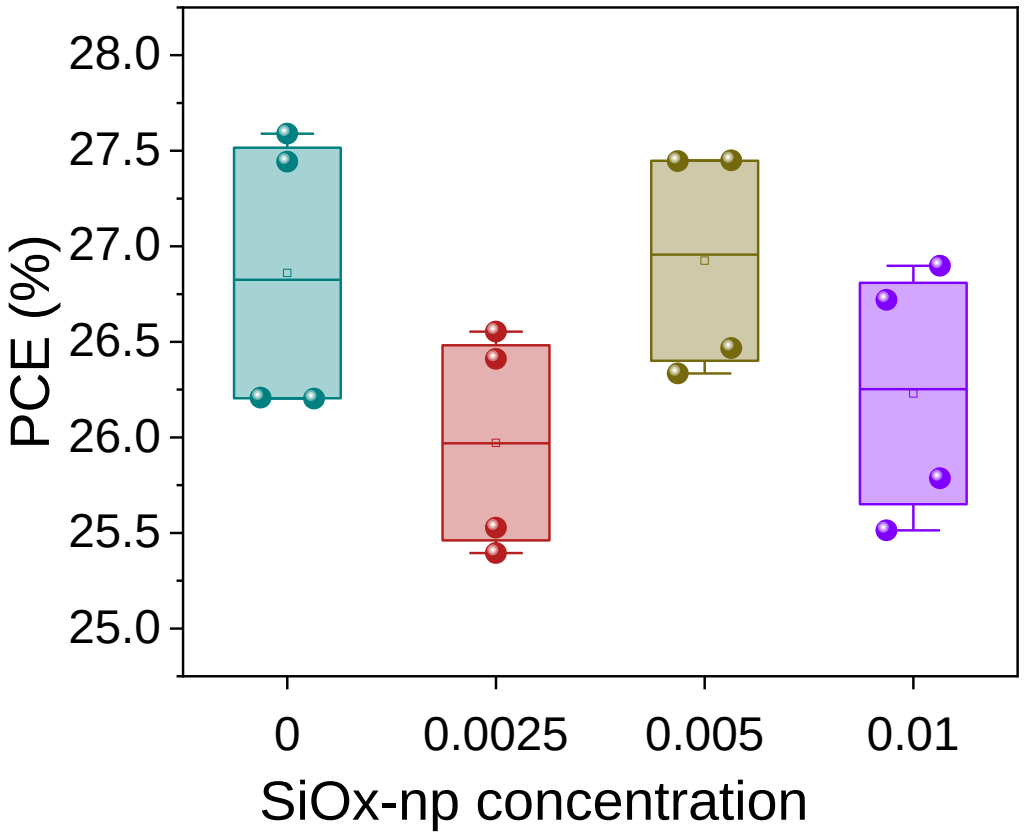

Figure S34. PCE of MBG-Si tandem devices with different concentrations of middle-reflector.

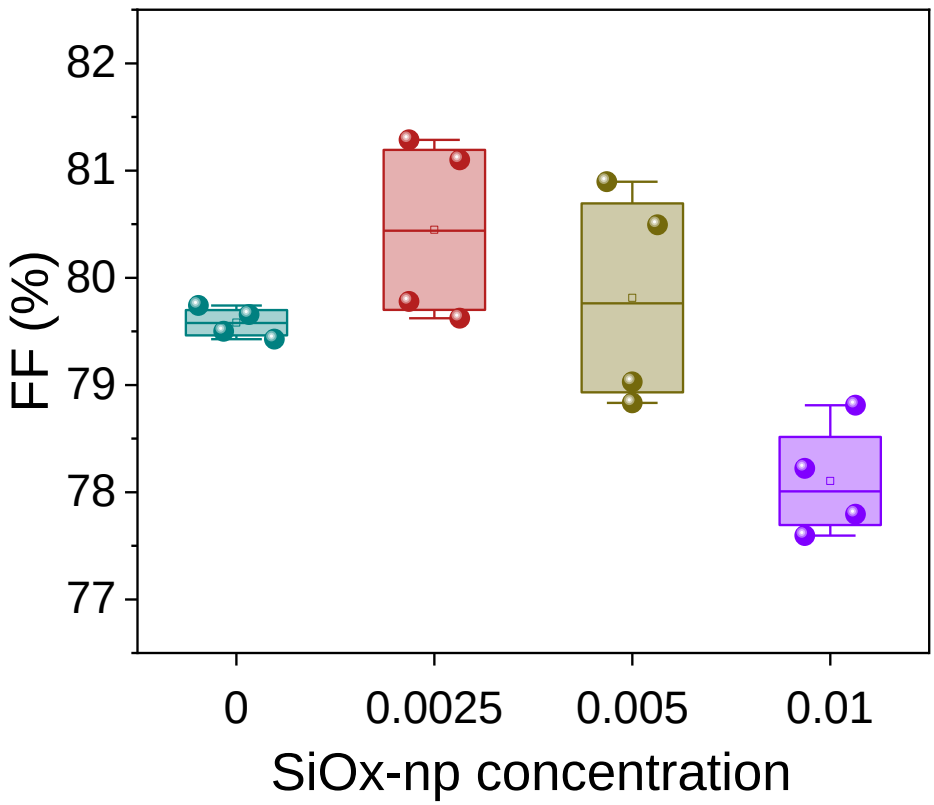

Figure S35. FF of MBG-Si tandems with different concentrations of middle-reflector.

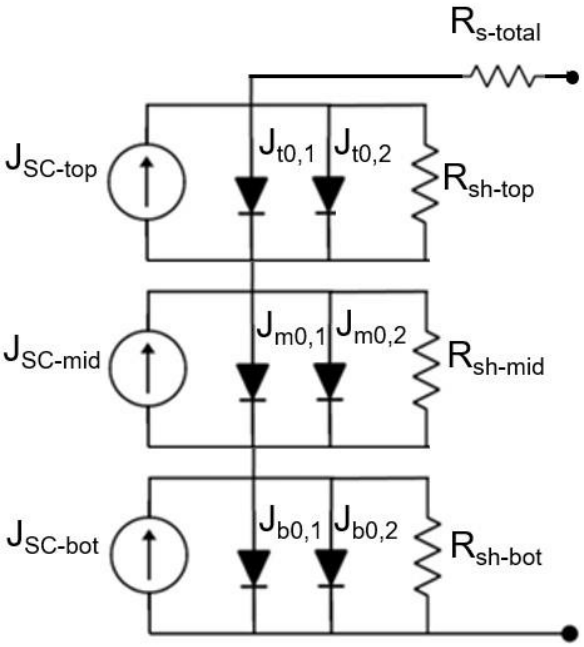

Rs-total (ohm.cm^2)	Rsh-top (ohm.cm^2)	Jt 0,1 (A/cm^2)	Jt 0,2 (A/cm^2)	Rsh-mid (ohm.cm^2)	Jm 0,1 (A/cm^2)	Jm 0,2 (A/cm^2)	Rsh-bot (ohm.cm^2)	Jb 0,1 (A/cm^2)	Jb 0,2 (A/cm^2)
13.5	2×10^{3}	5×10^{-21}	1×10^{-14}	1×10^{5}	5×10^{-18}	1×10^{-14}	5×10^{5}	3×10^{-14}	1×10^{-11}

Figure S36. 3J Equivalent circuit model and the parameters utilized for numerical calculations.

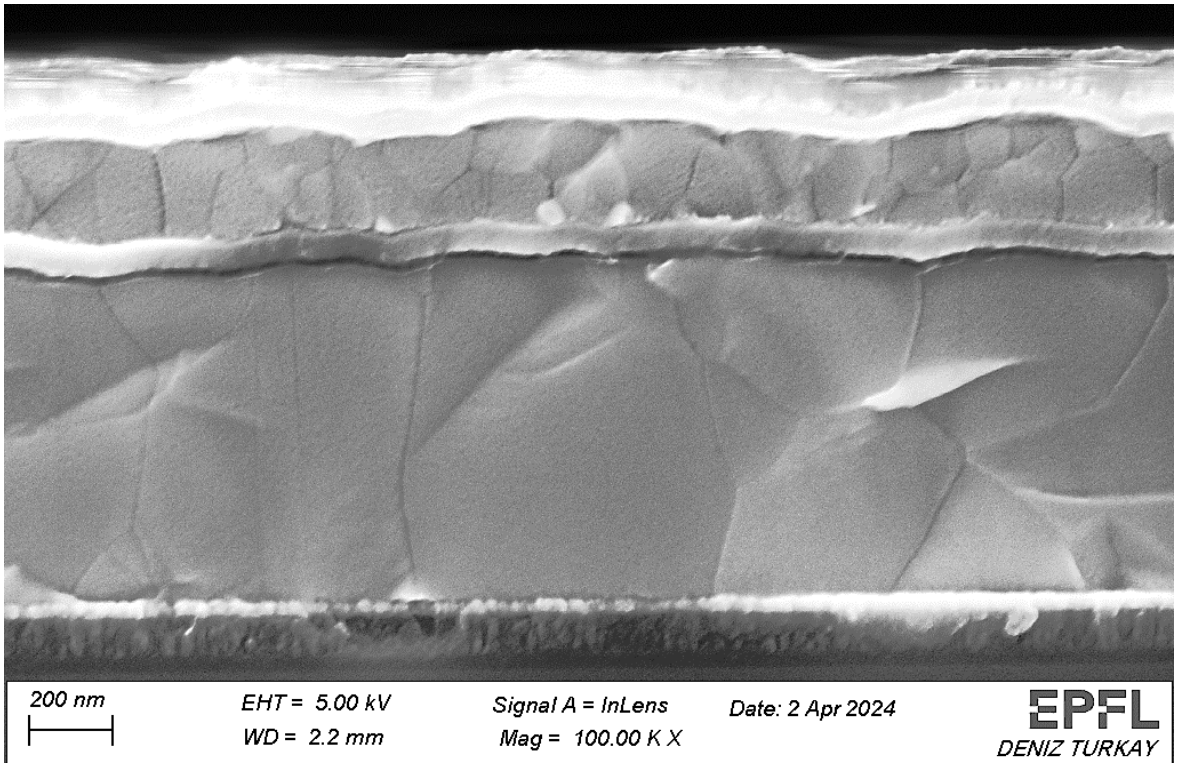

Figure S37. Cross-section SEM image of a triple-junction device on a front-flat Si.

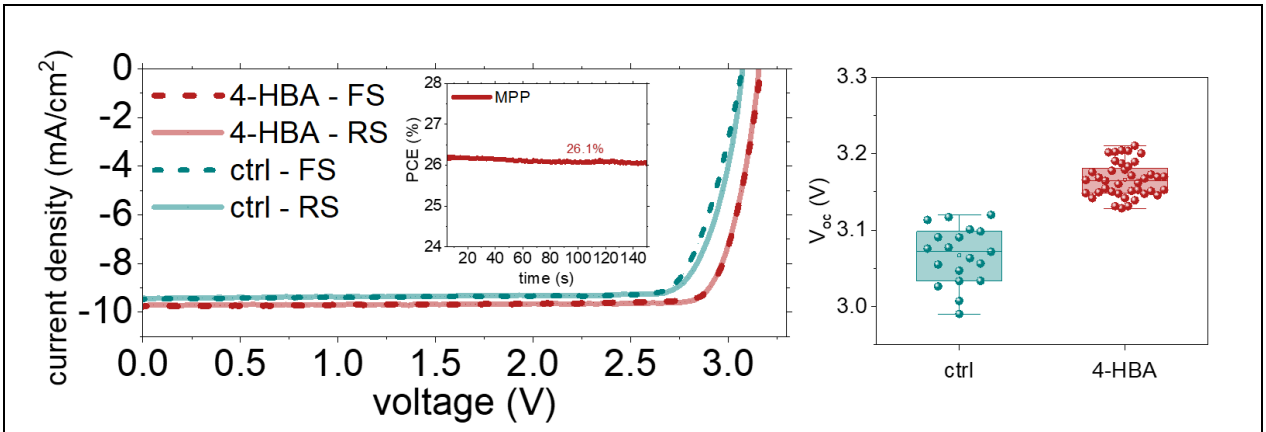

Figure S38. 3J device results with and without 4-HBA additive, prior to optical improvements in the middle cell. Both reverse and forward scan included.

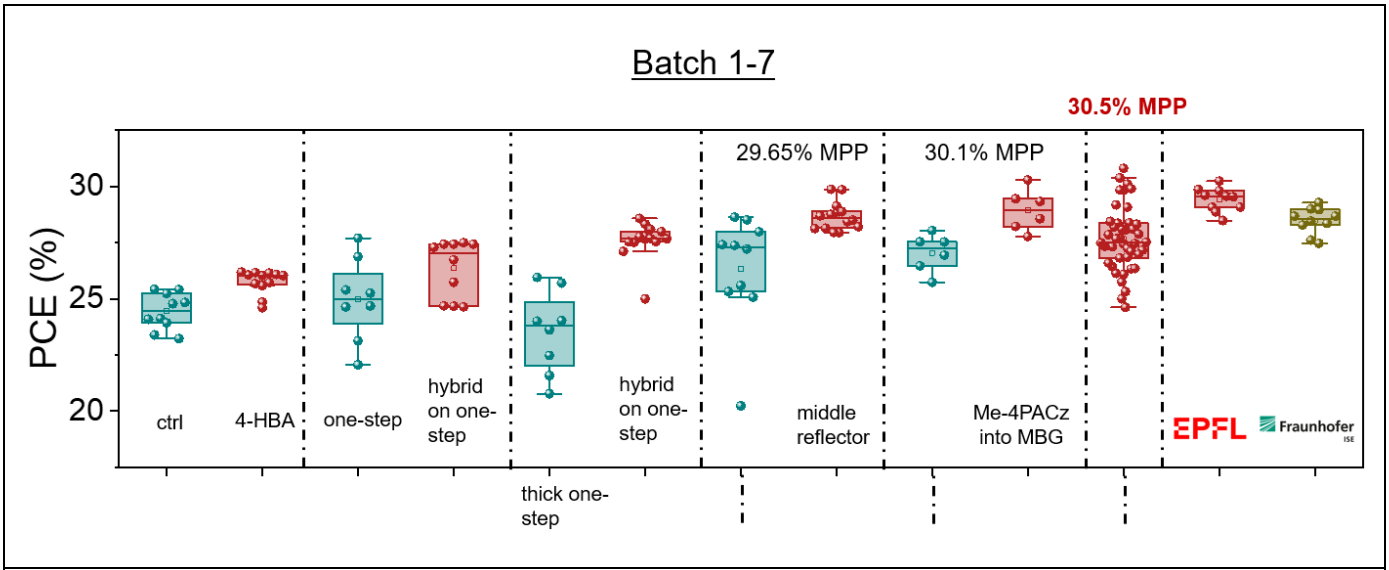

Figure S39. Device performance along 7 batches of fabrications with different conditions were tested. 1st batch is on front-flat Si bottom-cells, and the rest of the batches utilize double-side nanotextured bottom cells.

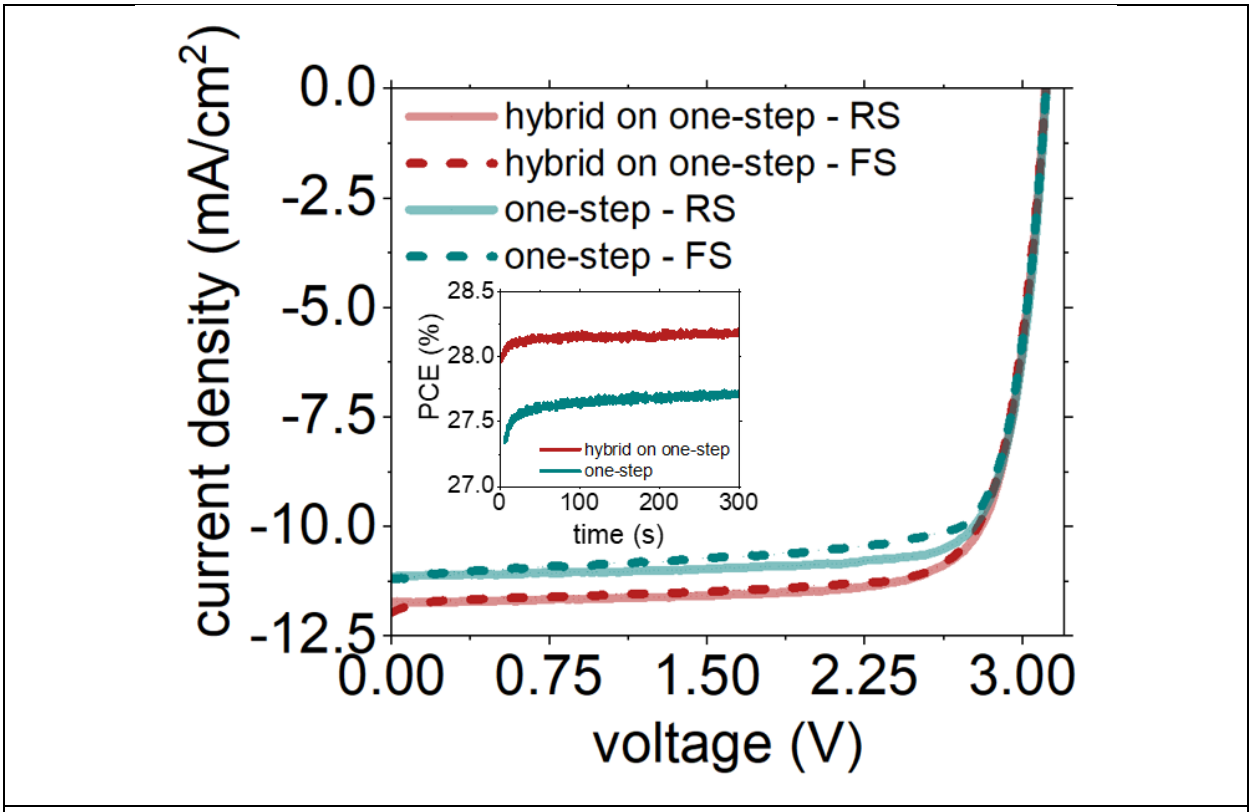

Figure S40. Reverse and forward scan curves of one-step and three absorber comparisons in Batch 2 (inset shows MPP).

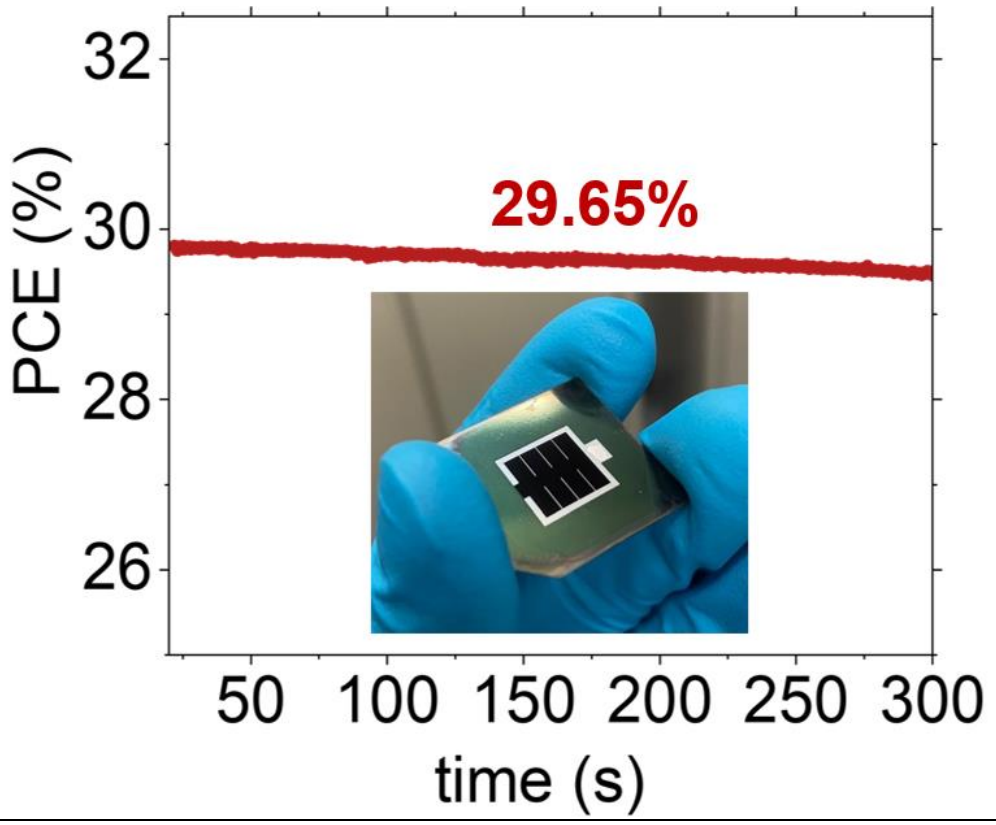

Figure S41. MPP tracking for the champion cell from batch 4.

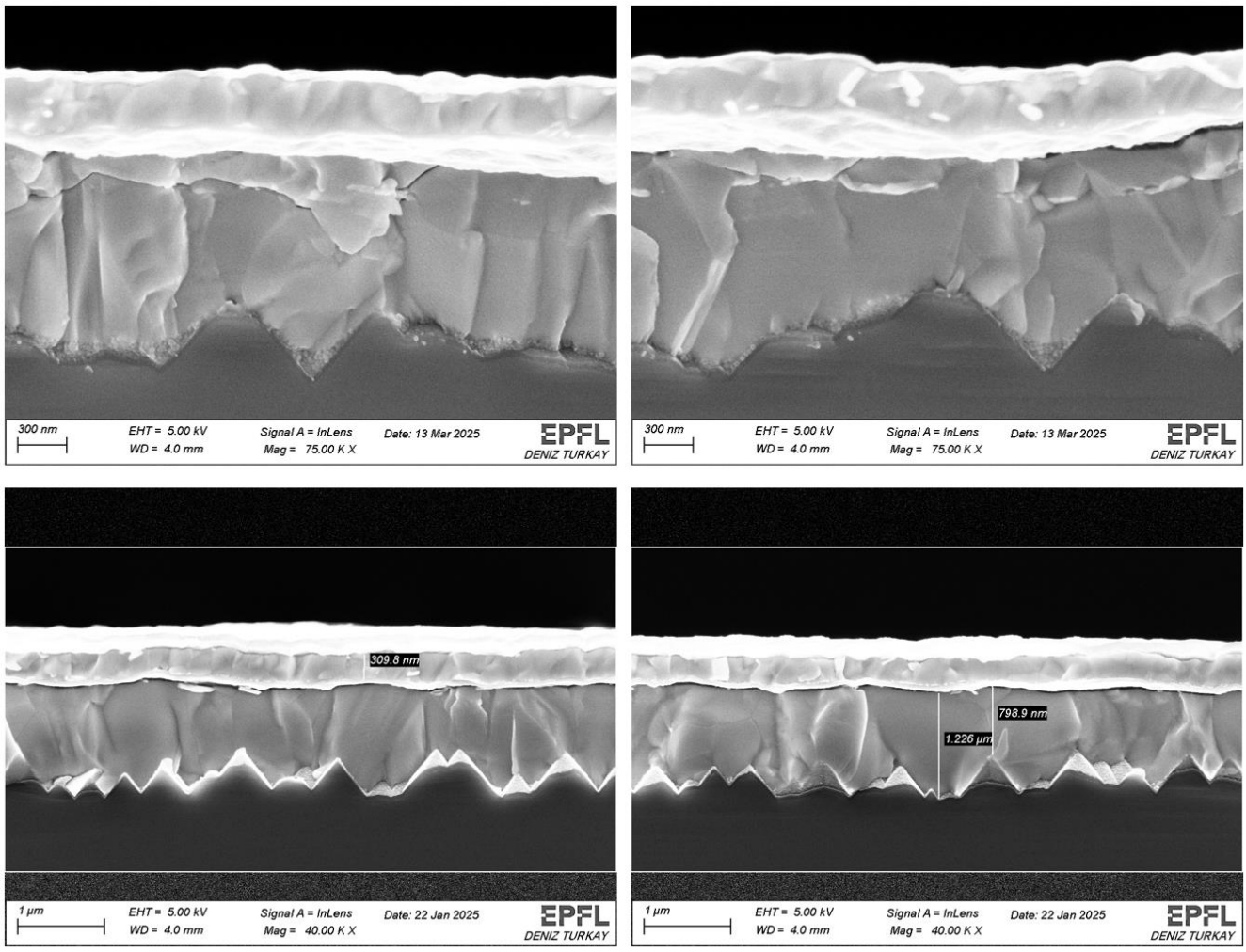

Figure S42. Cross-section SEM image of a triple-junction device on nanotextured Si.

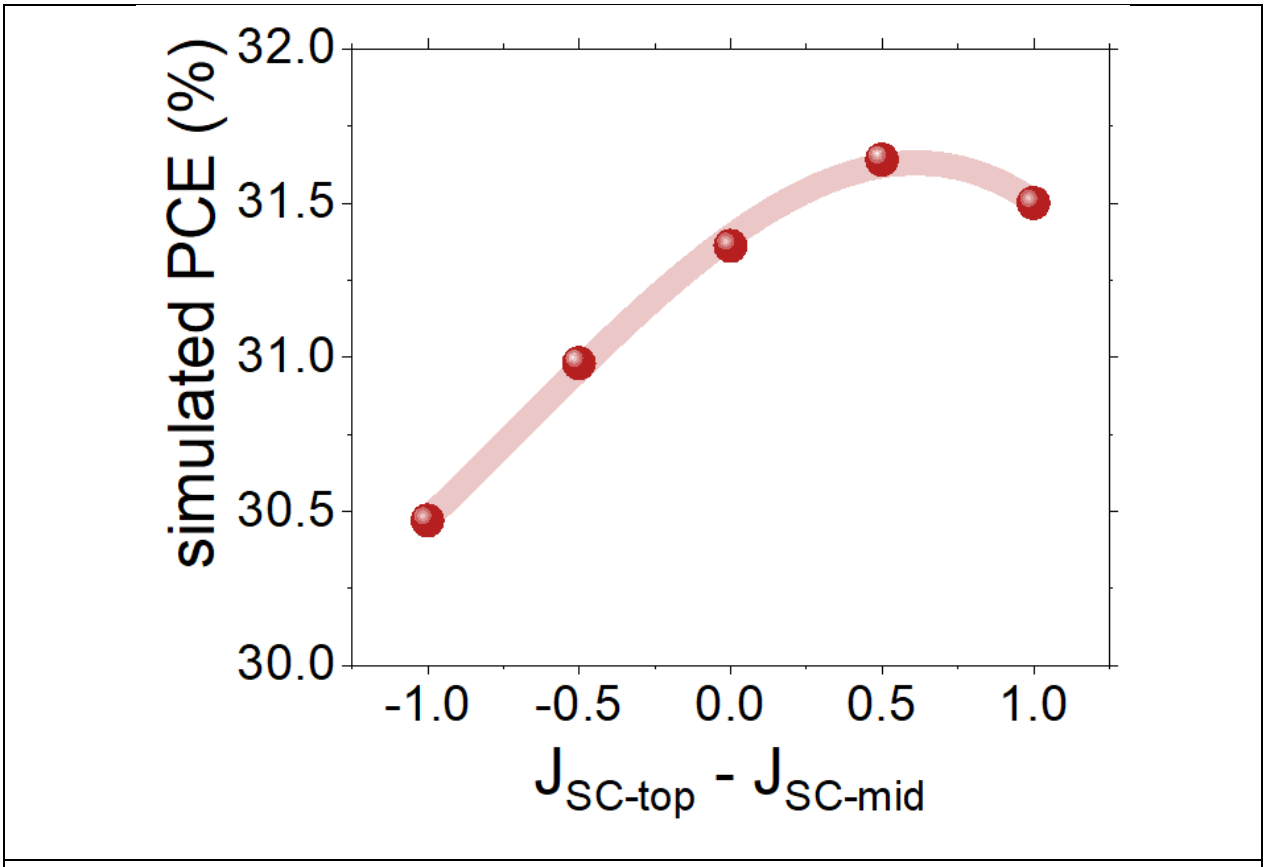

Figure S43. Simulated PCE from circuit modeling with changing mismatch conditions between top and middle-cell. Optimum performance is achieved at 0.5 mA/cm^2 middle limiting scenario.

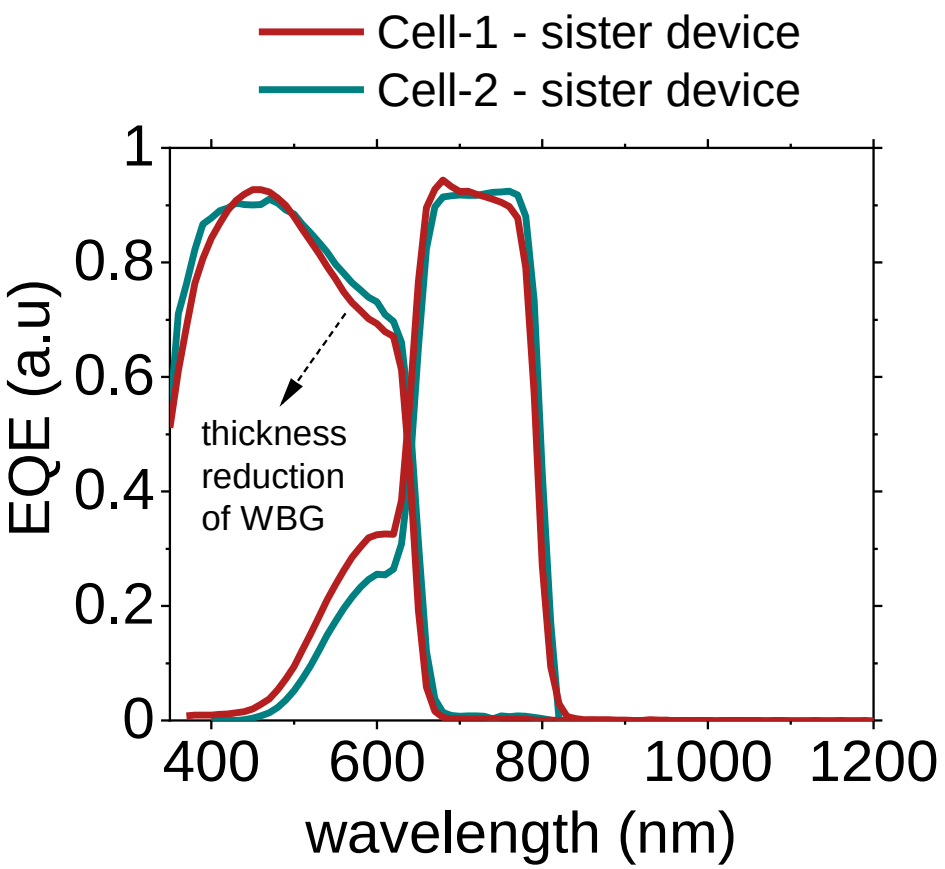

Figure S44. Representative EQE of top and middle-cell for triple-junctions from Batch 5 (same batch as Cell-1) and Batch 6 (same batch as Cell-2), showing decreasing thickness of the top-cell to improve current matching.

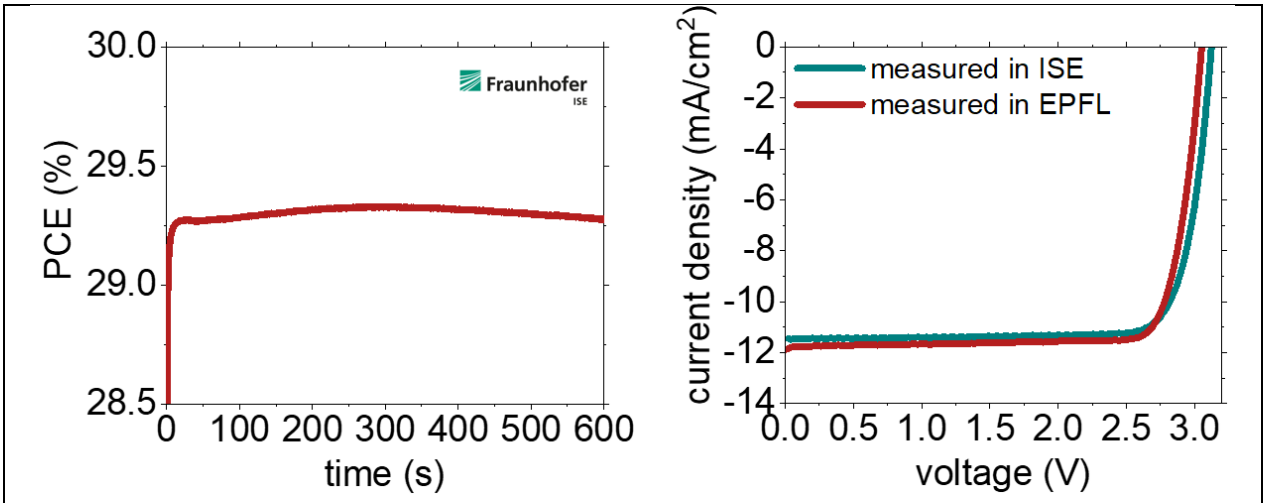

Figure S45. PCE tracking (at fixed voltage) of the champion device measured in Fraunhofer ISE and the comparison of JVs of the same device measured in ISE and EPFL.

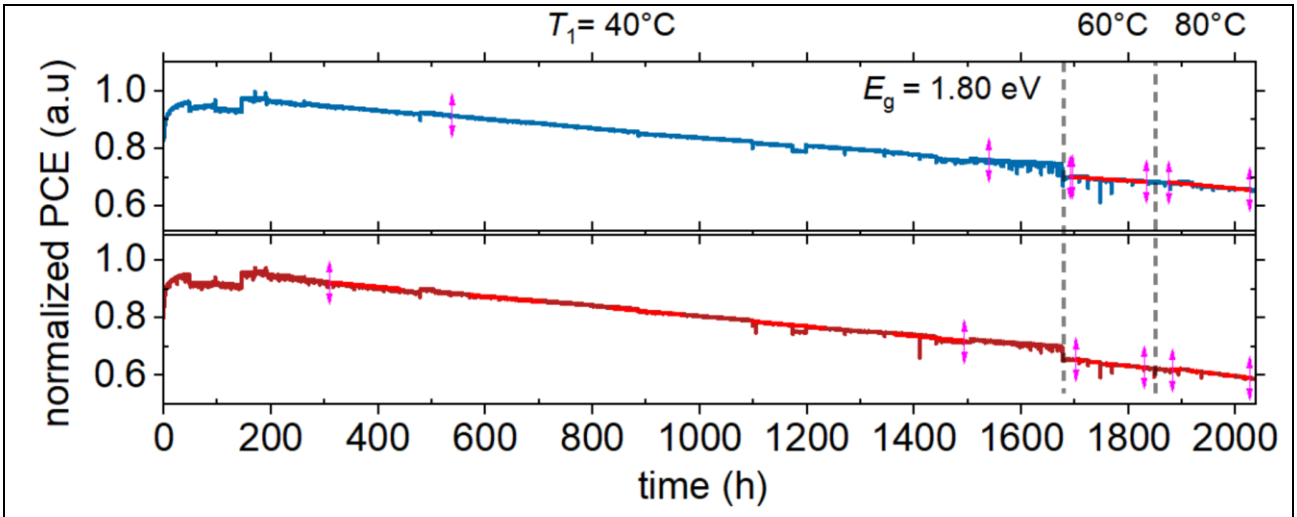

Figure S46. MPP tracking of single junction devices with WBG absorber, control (blue) and 4-HBA (red). The fit regions to extract the degradation rate.

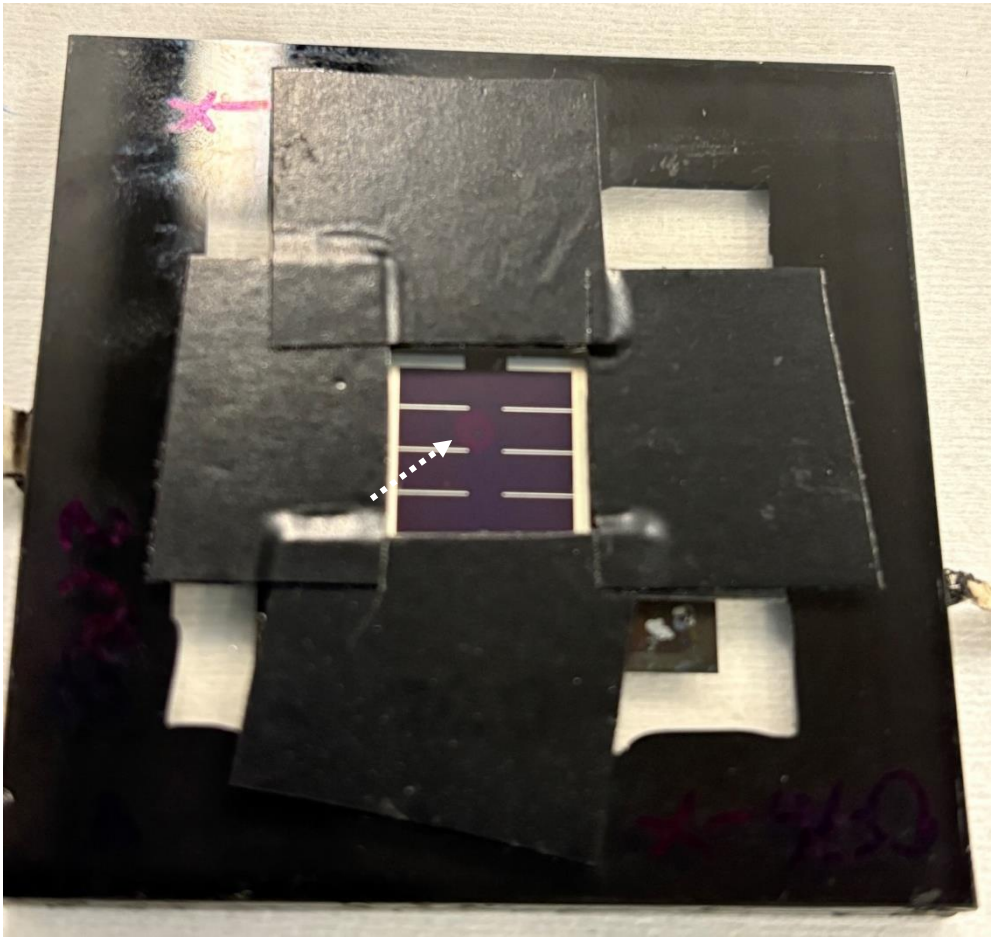

Figure S47. Image of the encapsulated 3J device after 500h of DH testing that lost 22.9 $\%_{rel}$ PCE. In the middle of the sample, yellow point formation due to degradation is observed.

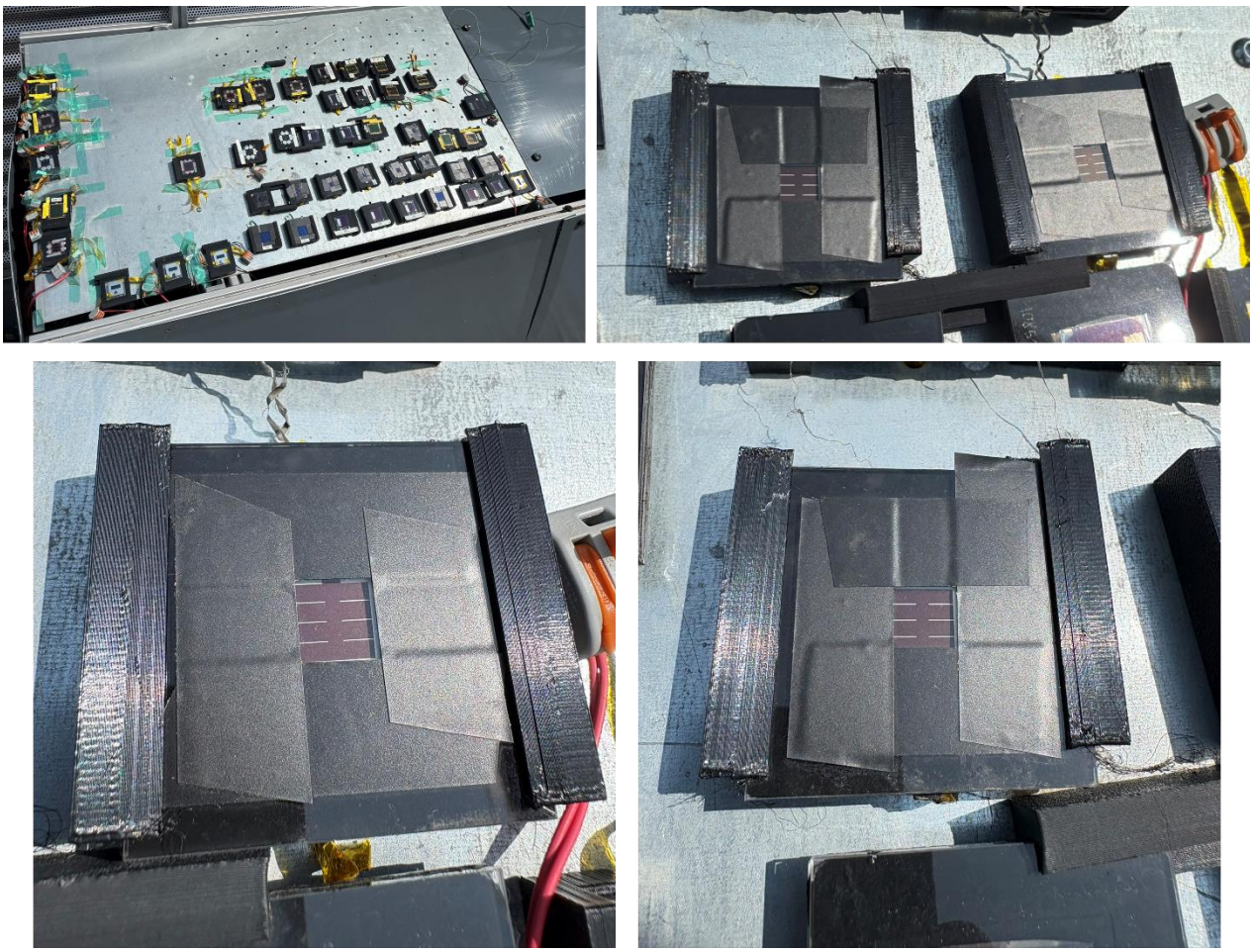

Figure S48. Images of the outdoor monitoring setup and tracked cells taken on the 6th of June, 2025. No visible degradation is observed in the 3J devices.

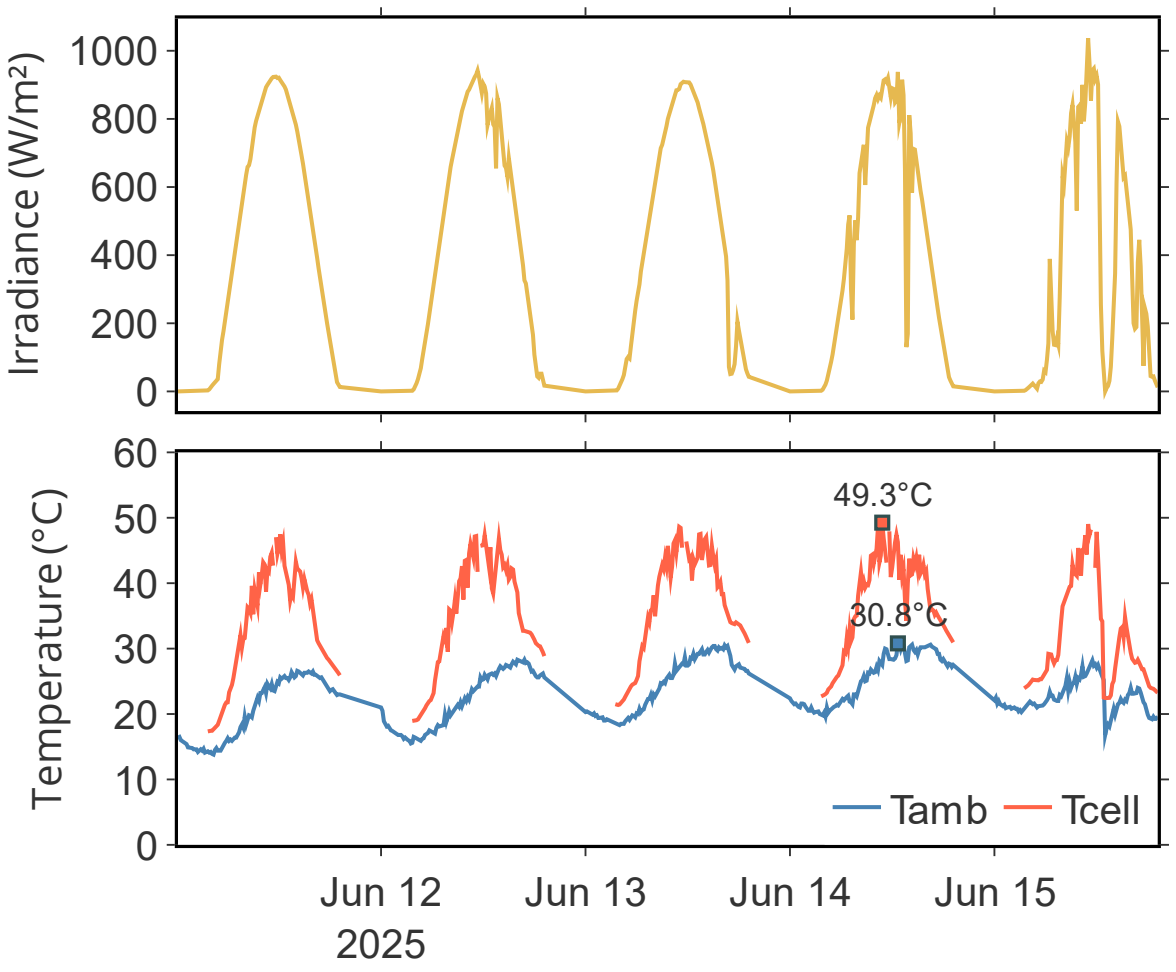

Figure S49. Measured cell temperature using a thermocouple behind a sister-cell and ambient temperature. Before 29 May, no data was recorded for the cell temperature due to technical difficulty. Cell temperature is ~19 °C higher than ambient temperature at peak irradiation.

References

1. D. Turkay, K. Artuk, X.-Y. Chin, D. A. Jacobs, S.-J. Moon, A. Walter, M. Mensi, G. Andreatta, N. Blondiaux, H. Lai, F. Fu, M. Boccard, Q. Jeangros, C. M. Wolff, C. Ballif, Synergetic substrate and additive engineering for over 30%-efficient perovskite-Si tandem solar cells. *Joule*, doi: 10.1016/j.joule.2024.04.015 (2024).
2. L. Antognini, V. Paratte, J. Haschke, J. Cattin, J. Dreon, M. Lehmann, L. Lou Senaud, Q. Jeangros, C. Ballif, M. Boccard, Influence of the Dopant Gas Precursor in P-Type Nanocrystalline Silicon Layers on the Performance of Front Junction Heterojunction Solar Cells. *IEEE J Photovolt* **11**, 944–956 (2021).
3. G. Kresse, D. Joubert, From ultrasoft pseudopotentials to the projector augmented-wave method. *Phys Rev B* **59**, 1758–1775 (1999).
4. G. Kresse, J. Furthmüller, Efficient iterative schemes for *ab initio* total-energy calculations using a plane-wave basis set. *Phys Rev B* **54**, 11169–11186 (1996).
5. J. Ning, M. Kothakonda, J. W. Furness, A. D. Kaplan, S. Ehlert, J. G. Brandenburg, J. P. Perdew, J. Sun, Workhorse minimally empirical dispersion-corrected density functional with tests for weakly bound systems: r ^{2} SCAN+rVV10. *Phys Rev B* **106**, 075422 (2022).
6. A. P. Bartók, J. R. Yates, Regularized SCAN functional. *J Chem Phys* **150** (2019).
7. J. W. Furness, A. D. Kaplan, J. Ning, J. P. Perdew, J. Sun, Accurate and Numerically Efficient r ^{2} SCAN Meta-Generalized Gradient Approximation. *J Phys Chem Lett* **11**, 8208–8215 (2020).
8. J. Sun, R. C. Remsing, Y. Zhang, Z. Sun, A. Ruzsinszky, H. Peng, Z. Yang, A. Paul, U. Waghmare, X. Wu, M. L. Klein, J. P. Perdew, Accurate first-principles structures and energies of diversely bonded systems from an efficient density functional. *Nat Chem* **8**, 831–836 (2016).
9. J. Sun, A. Ruzsinszky, J. P. Perdew, Strongly Constrained and Appropriately Normed Semilocal Density Functional. *Phys Rev Lett* **115**, 036402 (2015).
10. R. Sabatini, T. Gorni, S. de Gironcoli, Nonlocal van der Waals density functional made simple and efficient. *Phys Rev B* **87**, 041108 (2013).
11. O. A. Vydrov, T. Van Voorhis, Nonlocal van der Waals density functional: The simpler the better. *J Chem Phys* **133** (2010).
12. G. Makov, M. C. Payne, Periodic boundary conditions in *ab initio* calculations. *Phys Rev B* **51**, 4014–4022 (1995).
13. "IEC, Comission, International ELectrotechnical, Photovoltaic devices – Part 8-1: Measurement of spectral responsivity of multi-junction photovoltaic (PV) devices, 1st edn, 2017. ."
14. D. Chojniak, M. Schachtner, S. K. Reichmuth, A. J. Bett, M. Rauer, J. Hohl-Ebinger, A. Schmid, G. Siefer, S. W. Glunz, A precise method for the spectral adjustment of LED and multi-light source solar simulators. *Progress in Photovoltaics: Research and Applications* **32**, 372–389 (2024).
15. IEC, Comission, International ELectrotechnical, Photovoltaic devices – Part 1-1: Measurement of Current-Voltage Characteristics of Multi-Junction Photovoltaic (PV) Devices, 1st edn, 2017.
16. M. Meusel, R. Adelhelm, F. Dimroth, A. W. Bett, W. Warta, Spectral mismatch correction and spectrometric characterization of monolithic III-V multi-junction solar cells. *Progress in Photovoltaics: Research and Applications* **10**, 243–255 (2002).

17. O. Fischer, A. D. Bui, F. Schindler, D. Macdonald, S. W. Glunz, H. T. Nguyen, M. C. Schubert, Versatile implied open-circuit voltage imaging method and its application in monolithic tandem solar cells. *Progress in Photovoltaics: Research and Applications*, doi: 10.1002/pip.3754 (2023).
18. G. Ashiotis, A. Deschildre, Z. Nawaz, J. P. Wright, D. Karkoulis, F. E. Picca, J. Kieffer, The fast azimuthal integration Python library: PyFAI. *J Appl Crystallogr* **48**, 510–519 (2015).
19. K. Momma, F. Izumi, *VESTA 3* for three-dimensional visualization of crystal, volumetric and morphology data. *J Appl Crystallogr* **44**, 1272–1276 (2011).
20. C. Liu, Y. Yang, H. Chen, J. Xu, A. Liu, A. S. R Bati, H. Zhu, L. Grater, S. Sudhakar Hadke, C. Huang, V. K. Sangwan, T. Cai, D. Shin, L. X. Chen, M. C. Hersam, C. A. Mirkin, B. Chen, M. G. Kanatzidis, E. H. Sargent, "Bimolecularly passivated interface enables efficient and stable inverted perovskite solar cells;" https://www.science.org.
21. Y. Yang, H. Chen, C. Liu, J. Xu, C. Huang, C. D. Malliakas, H. Wan, A. S. R Bati, Z. Wang, R. P. Reynolds, I. W. Gilley, S. Kitade, T. E. Wiggins, S. Zeiske, S. Suragtkhuu, M. Batmunkh, L. X. Chen, B. Chen, M. G. Kanatzidis, E. H. Sargent, "Amidination of ligands for chemical and field-effect passivation stabilizes perovskite solar cells;" https://www.science.org.
22. Q. Tan, Z. Li, G. Luo, X. Zhang, B. Che, G. Chen, H. Gao, D. He, G. Ma, J. Wang, J. Xiu, H. Yi, T. Chen, Z. He, Inverted perovskite solar cells using dimethylacridine-based dopants. *Nature* **620**, 545–551 (2023).